



# CHORUS

This is the accepted manuscript made available via CHORUS. The article has been published as:

## Enhanced ferroelectric and piezoelectric properties of BCT-BZT at the morphotropic phase boundary driven by the coexistence of phases with different symmetries

Smaranika Dash, Dhiren K. Pradhan, Shalini Kumari, Ravikant, Md. Mijanur Rahaman, C. Cazorla, Kumar Brajesh, Ashok Kumar, Reji Thomas, Philip D. Rack, and Dillip K. Pradhan

Phys. Rev. B **104**, 224105 — Published 16 December 2021

DOI: [10.1103/PhysRevB.104.224105](https://doi.org/10.1103/PhysRevB.104.224105)

# Enhanced ferroelectric and piezoelectric properties of BCT-BZT at the Morphotropic Phase Boundary driven by the coexistence of phases of different symmetries

Smaranika Dash<sup>1</sup>, Dhiren K. Pradhan<sup>2,3</sup>, Shalini Kumari<sup>4</sup>, Ravikant<sup>5</sup>, Md. Mijanur Rahaman<sup>6</sup>, C. Cazorla<sup>7</sup>, Kumar Brajesh<sup>8</sup>, Ashok Kumar<sup>9,10</sup>, Reji Thomas<sup>11,12</sup>, Philip D. Rack<sup>2,3</sup>, Dillip K. Pradhan<sup>1\*</sup>

<sup>1</sup> Department of Physics and Astronomy, NIT Rourkela, Rourkela, Odisha-769008, India

<sup>2</sup> Department of Materials science and Engineering, University of Tennessee, Knoxville, TN 37996, USA

<sup>3</sup> Center for Nanophase Materials Sciences, Oak Ridge National Laboratory, Oak Ridge, TN 37831, USA

<sup>4</sup> Department of Materials Science & Engineering, The Pennsylvania State University, University Park, Pennsylvania 16802, USA.

<sup>5</sup> Department of Physics, Government College Sailana, Vikram University, Ujjain, Madhya Pradesh 456010, India

<sup>6</sup> Departmental of Materials Science and Engineering, University of Rajshahi, Rajshahi 6205, Bangladesh

<sup>7</sup> Departament de Física, Universitat Politècnica de Catalunya, Campus Nord B4-B5, Barcelona E-08034, Spain

<sup>8</sup> Department of Material science and Engineering, Indian Institute of Technology Kanpur, Kanpur, 208016, India

<sup>9</sup> CSIR-National Physical Laboratory, Dr. K. S. Krishnan Marg, New Delhi-110012, India

<sup>10</sup> Academy of Scientific and Innovative Research (AcSIR), Ghaziabad-201002, India

<sup>11</sup> Division of Research and Development <sup>12</sup> School of Chemical Engineering and Physical Sciences, Lovely Professional University, Jalandhar-Delhi G.T. Road, Phagwara, Punjab—, 144411, India

## Abstract

The discovery of lead-free piezoelectric materials is crucial for future information and energy storage applications. Enhanced piezoelectric and other physical properties are commonly observed near the morphotropic phase boundary (MPB) composition of ferroelectric solid solutions. The  $(1-x)\text{Ba}(\text{Zr}_{0.2}\text{Ti}_{0.8})\text{O}_3-x(\text{Ba}_{0.7}\text{Ca}_{0.3})\text{TiO}_3$  (BZT- $x$ BCT) system exhibits a large electromechanical response around its MPB region at  $x=0.5$ . We report experimental and theoretical results of BZT- $x$ BCT over a wide composition range ( $0.3 \leq x \leq 1.0$ ). X-ray diffraction and Raman spectroscopy studies indicate a composition-induced structural phase transition from a rhombohedral ( $R3m$ ) phase at  $x \leq 0.4$  to a tetragonal ( $P4mm$ ) phase at  $x \geq 0.6$  through a multiphase coexistence region at  $0.45 \leq x \leq 0.55$  involving orthorhombic + tetragonal ( $Amm2+P4mm$ ) phases. First-principles calculations elucidate the phase competition in the

coexistence region. The critical composition ( $x=0.5$ ) displays enhanced dielectric, ferroelectric and piezoelectric properties, where notably  $d_{33} \sim 320$  pC/N. This work provides clear evidence of  $Amm2+P4mm$  crystallographic phases in the MPB region, which is responsible for the improved functional properties.

**Keywords:** Lead free ferroelectric oxide; Ferroelectricity; Piezoelectricity; Phase transition; MPB

---

\* Author for correspondence E-mail: dillip.pradhan79@gmail.com (Dr. Dillip K. Pradhan)

Tel: +91-661-2462729, Fax: +91-661- 2462999

## I. INTRODUCTION

Ferroelectric materials exhibit spontaneous and switchable electrical polarization, electro-optic, pyroelectric, and piezoelectric effects with strong electromechanical coupling [1,2]. This switchable polarization coupled with electronic transport properties, surface chemistry, and strain, enable additional multifunctional device possibilities. Due to the existence of these functional properties, ferroelectric materials have attracted significant attention to both fundamental scientific interests, as well as their potential applications in non-volatile memory, energy storage, energy harvesting, transducers, actuators, motors, sensors, thermal imaging and other multifunctional devices [2]. The current industries are dominated by Pb-based piezo-electric systems such as  $Pb(Zr_xTi_{1-x})O_3$  (PZT) ferroelectrics,  $(1-x)Pb(Mg_{1/3}Nb_{2/3}O_3)-xPbTiO_3$  (PMN- $x$ PT) relaxors [1–4]. The lead-based ferroelectric/piezoelectric systems are widely used in electromechanical devices due to their superior piezoelectric response. Most of the lead-based compounds contain more than 60 wt.% of toxic lead [2]. This hazardous toxic element is volatile in nature and released to the environment during processing. Thus, Pb recycling and disposal impose severe environmental and health concerns [3]. Policies have been enacted by various countries to restrict the use of toxic (Pb-based) materials in various electrical/electronic devices [4]. In addition, the volatility of lead during processing leads to non-stoichiometry and deterioration of the functional properties (like, polarization, piezoelectric constants, elastic constants) of devices [4,5]. In view of all these shortcomings, many research efforts are currently directed towards the discovery and design of lead-free materials with improved dielectric, ferroelectric and piezoelectric properties. Some of the promising lead free candidates are  $BaTiO_3$  (BT),  $K_{1-x}Na_xNbO_3$  (KNN), and  $Bi_{1/2}Na_{1/2}TiO_3$  (NBT) based materials [2,3]. Among them, KNN and NBT contains volatile elements like Bi, Na, K, which result in off-stoichiometry and poor densification that leads to degradation of physical properties [5]. Although BT is one of the important ferroelectric oxide, it possesses a relatively low piezoelectric coefficient ( $d_{33} \sim 200$  pC/N), which limits the device applications [6]. However, doped/modified BT based materials have received significant attention in recent years after the discovery of Ca and Zr doped BT, i.e,  $(1-x)Ba(Zr_{0.2}Ti_{0.8})O_3-x(Ba_{0.7}Ca_{0.3})TiO_3$  (BZT- $x$ BCT) for  $x=0.5$ , which exhibits giant piezoelectric response  $d_{33} \sim 620$  pC/N, exceeds that of many soft PZT based materials [7].

$BaTiO_3$  undergoes a sequence of structural phase transitions with temperature. With decreasing temperature, the paraelectric cubic phase  $Pm\bar{3}m$  transforms to the ferroelectric tetragonal ( $P4mm$ ) phase at  $\sim 130$  °C and below 130 °C the material remains in the ferroelectric state. Around 0 °C the tetragonal ( $P4mm$ ) phase changes to an orthorhombic

(*Amm*2) phase and around -90 °C this orthorhombic phase changes to a rhombohedral (*R3m*) phase. These two ferroelectric transitions are of first order in nature [3]. By doping/chemical modifications, different ferroelectric phases can be created in BT. In the case of ferroelectric solid solutions, compositional modifications can induce a structural transformation from one ferroelectric state to another state having different crystal symmetry. This structural instability is termed as inter-ferroelectric instability [8]. This inter ferroelectric instability lowers the energy barrier that separate the two ferroelectric phases, and it provides an easy path for the polarization rotation. Consequently, enhanced ferroelectric and piezoelectric response are typically observed around morphotropic phase boundary (MPB) compositions in ferroelectric solid solutions [9–12]. Hence, tailoring the physical properties in ferroelectric materials by inducing MPB compositions is an interesting approach for BT system. The 0.5BZT-0.5BCT system has been actively studied for the replacement of Pb-based ferroelectrics for device applications. However, the mechanisms responsible for the exceptionally high piezoelectric properties are still not fully understood.

The enhanced piezoelectric and ferroelectric properties in the BZT-*x*BCT systems have been investigated from the structural perspective and the origin of the enhancement have been explained by different theories and models (See Supplementary information for detailed table summarizing previous structural studies in Table SI [13]; see also Refs. [7,14–49]. The first phase diagram on this solid solution was reported by Liu and Ren [7], where the MPB with a triple point consisting of cubic *Pm* $\bar{3}$ *m*, rhombohedral (*R3m*) and tetragonal (*P4mm*) crystallographic phases was proposed. The enhanced piezo response was explained for the MPB composition due to this tri-critical point, which lead to a vanishing polarization anisotropy that facilitates the polarization rotation between tetragonal and rhombohedral phases [7]. The phase coexistence of rhombohedral and tetragonal phase composition was verified experimentally by M. C. Ehmke et al. [17] and A. B. Haugen et al. [26] based on high-resolution synchrotron XRD. This observation was confirmed by J. Gao et al. [29] using convergent beam electron diffraction (CBED) analysis. The phase diagram was further reinvestigated by Keeble et al. [20], using high resolution synchrotron XRD and they reported the existence of an intermediate orthorhombic phase between the rhombohedral and tetragonal phases, which was supported by Tian et al. [27] as well. Based on these finding it was suggested that phase coexistence regions are the convergent region instead of tri-critical point as first reported by Liu-Ren [7]. In a ferroelectric system, the region in the phase diagram where different phase boundaries (for example cubic-tetragonal, tetragonal-orthorhombic, orthorhombic-rhombohedral) converge is referred to as the convergent region [20]. The enhanced piezoelectric properties were attributed to the presence of the orthorhombic phase. Contrary to these reports, M. Acosta et al. reported that neither the triple point nor the phase convergence region can explain the enhanced piezo-electric properties in the BZT-BCT system [50]. Further J. Gao et al. posited the enhanced piezoelectric response is due to the reversible domain wall motion in BZT-BCT system based on the small field Rayleigh analysis and large field strain measurements [51]. G. Tutunuc et al. studied the origin of enhancement of the piezo-response in BZT-*x*BCT solid solutions using electric field dependent *in situ* XRD analysis and showed the presence of a 90° domain wall. The enhancement of electrochemical response and piezoelectric properties in BZT-*x*BCT was then attributed to this 90° domain wall [31].

A high resolution *in situ* transmission electron microscopy (TEM) study on the electrical poling driven structural transformation from *R3m* + *P4mm* to the *Amm*2 phase of a single domain of BZT-BCT system has been studied by H. Guo et al. [33]. The primary contribution such as structural instabilities along with the elastic softening due to the initial electrical poling-re-poling was found to be responsible for the enhanced piezoelectric properties [33].

Recently, K. Brajesh et al. studied the electric field and temperature driven structural phase transformation based on x-ray diffraction analysis on 0.5BZT-0.5BCT and reported the co-existence of three phases; tetragonal ( $P4mm$ ) + Orthorhombic ( $Amm2$ ) + rhombohedral ( $R3m$ ) phase at room temperature [34]. They argued that, the presence of structural heterogeneity gives rise to polar nano-regions as in the case of relaxor ferroelectric systems. Due to the presence of polar nano-region, field induced transformation and domain wall motion occurs and that was ascribed to the amplification of the piezo response. Based on the combined theoretical and experimental investigations, Acosta et al. [52] also reported that the enhanced piezo-electric properties originate at the phase boundary of the orthorhombic-tetragonal phase, due to reduced anisotropy energy, high polarization and elastic softening. Further, the structural investigation confirmed the presence of the orthorhombic (O) phase between rhombohedral (R) and tetragonal (T) phases [52]. Based on large scale atomistic simulations, Nahas et al. reported the existence of large polarization fluctuations in the orthorhombic phase due to the combined effect of flat free energy landscape, the fragmented local structure, and the stability of the orthorhombic phase for a narrow temperature range [53]. This polarization fluctuation/rotation through the orthorhombic (low symmetry) phase is responsible for the enhanced piezo response in the BZT- $x$ BCT system [53]. Akbarzadesh et al. investigated the phase diagram of BZT- $x$ BCT systems numerically using the classical Monte Carlo simulations and path integral Monte Carlo simulations [43]. They observed a quantum fluctuation induced orthorhombic phase and suggested the enhancement of the piezoelectric properties is due to the inhomogeneous local structure. Zhang et al. suggested the relaxor-like behaviour in BZT- $x$ BCT system is due to cation substitution of different ionic radii (at A and B-sites) which creates heterogeneous strain at a local length scale [39]. This local strain heterogeneity influences the elastic behaviour near the MPB and results in an adaptive nano-scale microstructure, which in turn enhances the piezoelectric response [39]. Recently A. Mondal et al. studied pressure dependent X-ray diffraction on 0.5BZT-0.5BCT composition and showed a mixed Orthorhombic ( $Amm2$ ) + tetragonal ( $P4mm$ ) phase at room temperature [47]. K. Datta reported the mechanism of enhancement of piezoelectric properties based on total neutron scattering and Raman scattering and presented a statistical description of the atomic level polar ordering in the BZT- $x$ BCT system [54]. The enhancement of the piezo response was described in terms of the increased interaction among the cations in a strained local environment. They also proposed that the presence of low symmetry crystal structures cannot be a universal concept for the enhancement of piezoelectric response in any ferroelectric solid solution around the MPB [54].

Despite of wide range of experimental and theoretical investigations on the BZT- $x$ BCT system, a clear picture has not been developed to explain the coexistence of the crystal structures and enhanced piezoelectricity around the MPB. Hence, it is very important to understand the mechanism behind the exceptional piezoelectric properties of the lead free BZT- $x$ BCT. A fundamental understanding of the structure-property relationships in BZT- $x$ BCT near the MPB region is necessary, both from an experimental and the theoretical point of view. To better understand the structure-property relationship (i.e., compositional driven structural phase transitions) in BZT- $x$ BCT, a systematic investigation on the structural driven phase transition of BZT- $x$ BCT ( $0.3 \leq x \leq 1.0$ ) is studied. X-ray diffraction and Raman scattering studies on the compositional induced structural phase transitions is expected to elucidate the evidence of the MPB region. Additionally, first-principles calculations based on density functional theory (DFT) were performed to theoretically describe phase competition in the multiphase system. Furthermore, we measure and correlate the enhancement of the dielectric, ferroelectric and piezoelectric properties with crystal structure around the MPB region and discuss relaxor behaviour of the system.

## II. EXPERIMENTAL DETAILS

Polycrystalline ceramics of  $(1-x)\text{Ba}(\text{Zr}_{0.2}\text{Ti}_{0.8})\text{O}_{3-x}(\text{Ba}_{0.7}\text{Ca}_{0.3})\text{TiO}_3$  (BZT- $x$ BCT) with  $x=0.3, 0.4, 0.45, 0.48, 0.5, 0.52, 0.55, 0.6, 0.7, 0.8, 0.9, 1.0$  were prepared using the auto combustion technique. Stoichiometric amounts of high purity  $\text{Ba}(\text{NO}_3)_2$ ,  $\text{Ca}(\text{NO}_3)_2 \cdot 4\text{H}_2\text{O}$ ,  $\text{ZrO}(\text{NO}_3)_2 \cdot x\text{H}_2\text{O}$ ,  $\text{Ti}[\text{OCH}(\text{CH}_3)_2]_4$  and urea were taken as raw materials for the synthesis. The urea was used as fuel (F) and above raw materials forms the oxidiser (O). The above precursors were mixed stoichiometrically for the desired composition with a minimum amount of distilled water while maintaining F/O ratio to 1. The detailed synthesis procedure was described elsewhere [55]. The samples were then calcined at  $900^\circ\text{C}$  for 6 hour. The calcined powder was then mixed with 3 wt. % polyvinyl alcohol (PVA) and pressed to form disks of 10 mm diameter at a pressure of  $6 \times 10^7 \text{ kg/m}^2$ . The green pellets were initially heated at  $600^\circ\text{C}$  for 1 hour to remove the binder, and finally sintered at an optimized temperature of  $1450^\circ\text{C}$  for 4 hours.

Room temperature XRD data were collected using a high-resolution x-ray diffractometer, (PANalytical X'Pert Pro MPD), with  $\text{Cu K}_\alpha$  radiation ( $\lambda = 1.5405\text{\AA}$ ). For the XRD measurement, sintered pellets were crushed into fine powders and sieved followed by a heat treatment at  $600^\circ\text{C}$  for 2 hours to release the intergranular stress present in the sample during the grinding process. Rietveld refinements of the XRD patterns were carried out using Full proof software package. The room temperature Raman spectra of the sintered samples were recorded by a Raman spectrometer (Horiba Jobin Yvon T64000 system) using a 532 nm laser in the frequency range of  $10\text{-}1000 \text{ cm}^{-1}$ . The surface morphology of the samples was recorded using a field emission scanning electron microscope (FESEM) (NOVA Nano SEM 450). Sintered pellets were coated with gold for collecting the SEM micrographs to minimize charging. The presence of different elements along with the elemental composition ratio was studied with the help of energy dispersive X-ray (EDS) attached to FESEM equipment. For electrical measurements, both sides of the pellets were coated with silver paint and further dried at  $200^\circ\text{C}$  for 2 hours. The dielectric properties were measured at a temperature range from room temperature to  $500^\circ\text{C}$  in the frequency range of 100 Hz to 1 MHz using an impedance analyzer (HIOKI IM3570) with an oscillating voltage of 1 V. The room temperature ferroelectric hysteresis loops (P-E) were collected using Ferroelectric loop tester (Radiant Ferroelectric Tester) at a frequency of 10 Hz. The silver electroded samples were subjected to electrical poling at an applied DC electric field of 20 kV/cm at room temperature in a silicon oil bath prior to the PE loop measurement. The piezoelectric coefficient ( $d_{33}$ ) was measured using a YE2730A  $d_{33}$  meter after electrical poling.

The energetic and structural properties of lead-free BZT- $x$ BCT ceramics were calculated with first-principles methods based on density functional theory (DFT). We used the PBE variant of the generalised gradient approximation to DFT [56] as it is implemented in the VASP package [57,58]. The “projector augmented wave” method was employed to represent the ion cores [59], and we considered the following valence electrons: Ba  $5s, 5p$ , and  $6s$ ; Ca  $3s, 3p$ , and  $4s$ ; Ti  $3p, 4s$ , and  $3d$ ; Zr  $4s, 4p, 5s$  and  $4d$ ; and O  $2s$  and  $2p$ . Wave functions were represented in a plane-wave basis truncated at 650 eV. We used a 40-atoms simulation cell (equivalent to a  $2 \times 2 \times 2$  replication of the typical 5-atom perovskite unit cell in which the usual ferroelectric and anti-ferrodistortive distortions occurring in oxide compounds could be reproduced [60–63]. For integrations within the first Brillouin zone, we adopted a Gamma-centered k-point grid of  $6 \times 6 \times 6$ . Geometry relaxations were performed by using a conjugate-gradient algorithm that optimized the volume and shape of the simulation cell as well as the atomic positions. The imposed tolerance on the atomic forces was of  $0.01 \text{ eV} \cdot \text{\AA}^{-1}$ . By using these parameters, we obtained total energies that were converged to within

0.5 meV per f.u.. In order to provide meaningful comparisons with the experiments, in our DFT calculations we considered four different system compositions:  $\text{Ba}_6\text{Ca}_2\text{Ti}_8\text{O}_{24}$  (referred to as “ $x=1.00$ ”),  $\text{Ba}_7\text{Ca}_1\text{Ti}_7\text{Zr}_1\text{O}_{24}$  (referred to as “ $x=0.50$ ”),  $\text{Ba}_7\text{Ca}_1\text{Ti}_6\text{Zr}_2\text{O}_{24}$  (referred to as “ $x\approx 0.50$ ”) and  $\text{Ba}_8\text{Ti}_6\text{Zr}_2\text{O}_{24}$  (referred to as “ $x=0.00$ ”). Four different polymorphs were analysed for each composition, namely, tetragonal (polar, space group  $P4mm$ ), cubic (non-polar, space group  $Pm3m$ ), rhombohedral (polar, space group  $R3m$ ), and orthorhombic (polar, space group  $Amm2$ ).

### III. RESULTS

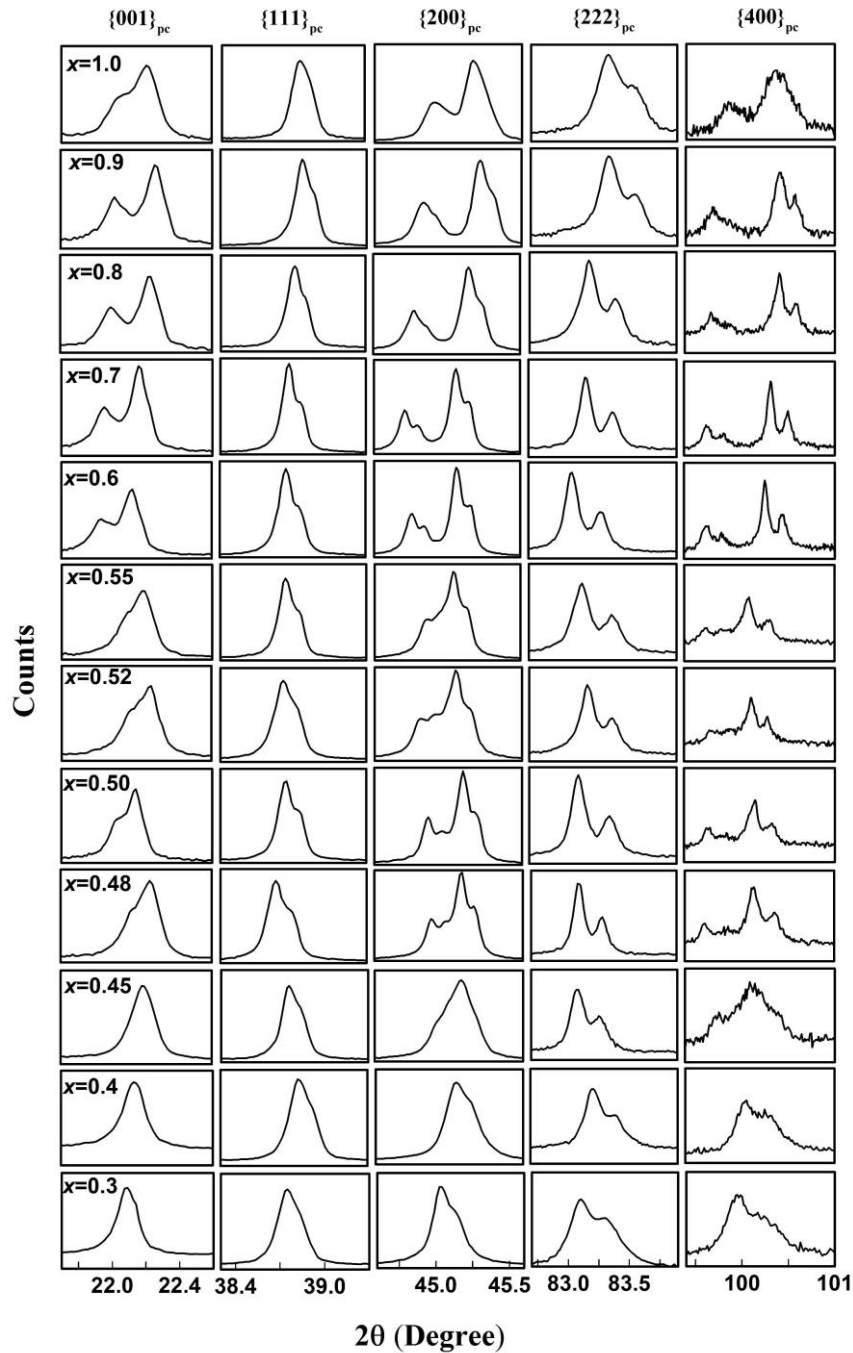
#### A. X-Ray Diffraction

Figure 1 represents the compositional evolutions of the XRD profile for the five pseudo-cubic (pc) reflections  $\{0\ 0\ 1\}_{pc}$ ,  $\{1\ 1\ 1\}_{pc}$ ,  $\{2\ 0\ 0\}_{pc}$ ,  $\{2\ 2\ 2\}_{pc}$ , and  $\{4\ 0\ 0\}_{pc}$  for the entire composition range of BZT- $x$ BCT ferroelectric materials. The XRD profiles presented here contains  $K\alpha_2$  ( $=1.54439\ \text{\AA}$ ) reflections apart from the main  $K\alpha_1$  ( $\lambda=1.5405\text{\AA}$ ) reflection. The distinct change in the pseudo-cubic reflections suggests a composition induced structural phase transition. The Rietveld refinement analysis was carried out to ascertain the exact nature of this structural phase transitions and the starting model for the refinement was proposed based on a visual analysis of the XRD spectra. Scrutiny of the splitting of the characteristic pseudo-cubic reflections  $\{h\ 0\ 0\}_{pc}$ ,  $\{h\ h\ 0\}_{pc}$ , and  $\{h\ h\ h\}_{pc}$  is the best way to identify the presence of tetragonal, orthorhombic and rhombohedral phases. All the pseudo-cubic reflections are singlet for cubic symmetry. For the tetragonal crystal structure, the pseudo-cubic reflections are characterized by the splitting of the  $\{h\ 0\ 0\}_{pc}$  reflection into doublets and the  $\{h\ h\ h\}_{pc}$  appears to be singlet. However, in the case of rhombohedral crystal structure reverse behaviour is expected i.e.,  $\{h\ h\ h\}_{pc}$  reflections are doublets and  $\{h\ 0\ 0\}_{pc}$  reflections are singlet. In the case of the orthorhombic crystal structure, splitting of both the  $\{h\ h\ h\}_{pc}$  and  $\{h\ 0\ 0\}_{pc}$  reflections is expected. Weak distortions in the structure are difficult to visualize in the lower order reflections (at lower angles) and hence higher order reflections (at higher angles) were considered. However, the intensity of higher order reflections is considerably weaker compared to the lower order reflections. In the present case, the peak to background ratio and resolution of our diffractions data is sufficient to identify different crystallographic phases (tetragonal, orthorhombic and rhombohedral) explicitly.

The singlet nature of the  $\{1\ 1\ 1\}_{pc}$  reflections and doublet nature of  $\{2\ 0\ 0\}_{pc}$  reflection suggests the tetragonal crystal structure for  $x=1.0$ . Detailed information can be obtained by carefully analysing the higher order reflections, so reflections such as  $\{2\ 2\ 2\}_{pc}$  and  $\{4\ 0\ 0\}_{pc}$  are also plotted and shown in Fig. 1. For pure BCT ( $x=1.0$ ), the doublet nature of the  $\{4\ 0\ 0\}_{pc}$  reflection and singlet  $\{2\ 2\ 2\}_{pc}$  reflection confirms the tetragonal crystal structure with space group  $P4mm$ . With an increase in the BZT concentration, the doublet  $\{4\ 0\ 0\}_{pc}$  and singlet  $\{2\ 2\ 2\}_{pc}$  reflection is maintained up to  $x=0.60$ . So, the XRD data were fitted using a Rietveld refinement technique with a single phase  $P4mm$  crystal structure ( $0.6\leq x\leq 1.0$ ) and a representative Rietveld refinement pattern for  $x=1.0$  is shown in Fig. 2(a). In order to have better clarity we have compared the fitted data for higher order reflections, which are shown as an inset of Fig. 2. There is good agreement between the experimental and the fitted data. The refined structural parameters obtained from Rietveld refinement for  $x=1.0$  are shown in Table SII (See Supplementary information) [13].

With an increase in the concentration of BZT, there is a distinct change in the pseudocubic diffraction pattern for  $x=0.55$  and then for  $x=0.40$  (Fig. 1). Thus, based on visual inspection of the pseudocubic diffraction pattern, there are distinct structures for the composition ranges  $0.3\leq x\leq 0.4$ ,  $0.45\leq x\leq 0.55$  and  $0.6\leq x\leq 1.0$ . For the composition  $x=0.3$  and  $0.4$ , the pseudo cubic

$\{4\ 0\ 0\}_{pc}$  profile is singlet (Fig. 1), which suggest the presence of Rhombohedral ( $R3m$ ) rather than tetragonal or orthorhombic phases.



**FIG. 1.** Evolution of pseudocubic Bragg profiles of  $\{0\ 0\ 1\}_{pc}$ ,  $\{1\ 1\ 1\}_{pc}$ ,  $\{2\ 0\ 0\}_{pc}$ ,  $\{2\ 2\ 2\}_{pc}$ ,  $\{4\ 0\ 0\}_{pc}$  obtained from room temperature X-ray powder diffraction of BZT- $x$ BCT with  $0.3 \leq x \leq 1.0$ .

Further, Rietveld refinements of the XRD patterns for  $x=0.4$ , with both  $R3m$  and  $Amm2$  space group has been carried out (Figs. 2(d) and 2(e)), where the best fitting is observed for the  $R3m$  space group, confirming rhombohedral structure for this compositional ranges. However, for  $x=0.55$ , the Rietveld refinement using  $P4mm$  space group resulted in a poor fit as the shape of the  $\{4\ 0\ 0\}_{pc}$  reflection is significantly modified due to the appearance of a

new peak in between the two tetragonal peaks. Actually,  $\{4\ 0\ 0\}_{pc}$  reflections of both the  $Amm2$  and  $P4mm$  structure are doublets. So, the presence of the extra reflections along with the  $P4mm$  tetragonal phase suggests the co-existence of those two phases in  $x=0.55$  composition. The pseudocubic  $\{4\ 0\ 0\}_{pc}$  reflections of the tetragonal phase, namely,  $(004)_T$  and  $(400)_T$  shows doublets at the extreme ends. As can be seen from Fig. 2, along with the doublet nature for the tetragonal distortions, the presence of peaks in the middle (between the tetragonal peaks) correspond to the orthorhombic structure (marked as O). It has been observed that the intensity of the orthorhombic ( $Amm2$ ) phase increases with a decrease in the BCT concentrations from  $x=0.55$  to 0.45. The increasing intensity of the orthorhombic (O) peak in between the tetragonal peak confirms the increasing fraction of the  $Amm2$  phase.

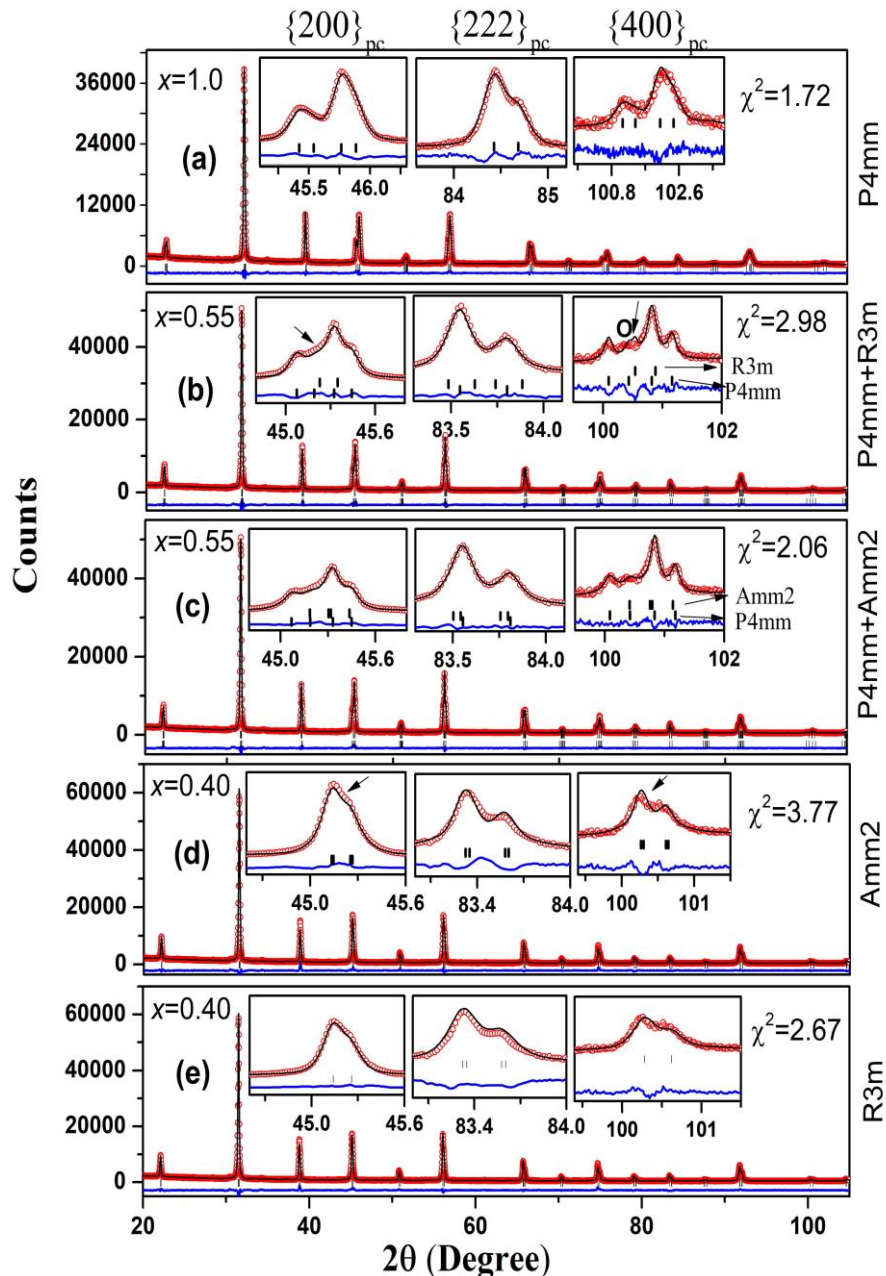


**FIG. 2.** Rietveld fitted XRD pattern of BZT-xBCT for (a)  $x=1.0$  using  $P4mm$  model (b, c)  $x=0.55$  using  $P4mm+R3m$  and  $P4mm+Amm2$  model (d, e)  $x=0.4$  using  $Amm2$  and  $R3m$  model. The inset shows the enlarged view of high quality of fit with selected Bragg profiles.

Since some of the peaks are not fit with  $P4mm$  structure for  $x=0.55$ , a different co-existence structural model was considered. Here pure BCT ( $x=1.0$ ) to BZT- $x$ BCT ( $x=1.0$  to  $x=0.6$ ) crystallizes in the  $P4mm$  crystal structure, whereas  $x=0.3$  and  $x=0.4$ , belongs to the rhombohedral crystal structure ( $R3m$ ). Since the composition  $x=0.55$  is expected to be the cross over from  $P4mm$  to ( $P4mm + Amm2$ ), different models (i) single phase tetragonal ( $P4mm$ ) structure, (ii) single phase orthorhombic ( $Amm2$ ) structure, (iii) tetragonal ( $P4mm$ ) + rhombohedral ( $R3m$ ) structure, and (iv) tetragonal ( $P4mm$ ) + orthorhombic ( $Amm2$ ) structure were fit to the powder XRD data using a Rietveld refinement. In case of the BT based ferroelectric system, the identification of the rhombohedral and orthorhombic phase is difficult due to similar pseudo cubic lattice parameters [36].

The fitted results for ( $P4mm + R3m$ ) and ( $P4mm + Amm2$ ) co-existence model are shown in Figs. 2(b) and 2(c) for  $x=0.55$ . The insets of the figure shows the magnified fitted plot of higher angle pseudo cubic reflections  $\{2\ 0\ 0\}_{pc}$ ,  $\{2\ 2\ 2\}_{pc}$ ,  $\{4\ 0\ 0\}_{pc}$ . The subtle misfit regions (indicated by arrow mark in the magnified pseudocubic  $\{2\ 0\ 0\}_{pc}$  and  $\{0\ 0\ 4\}_{pc}$  reflections) are observed for the refined ( $P4mm + R3m$ ) phases for  $x=0.55$ . Among the different structural model, the tetragonal and orthorhombic ( $P4mm + Amm2$ ) co-existence model gives the best fit. The refined structural parameters obtained from Rietveld refinement for  $x=0.55$  are shown in Table SIII [13]. Due to the addition of  $Amm2$  to the  $P4mm$  model, the software attempts to obtain the best fit by increasing the width of the Bragg peaks. This way additional intensity due to another phase is compensated. So, the ( $P4mm + Amm2$ ) phase co-existence model was extended up to  $x=0.45$  and a best fit was observed. In short, the co-existence of the  $P4mm$ - $Amm2$  ferroelectric crystallographic phases is the best way to explain the appearance of the orthorhombic phase along with tetragonal phase as observed in the XRD pattern (i.e., triplet nature of  $\{2\ 0\ 0\}_{pc}$  and  $\{4\ 0\ 0\}_{pc}$  diffraction profile). Although, the visual observation suggests that  $x=0.4$  is the rhombohedral crystal structure, we have fitted with both the orthorhombic and rhombohedral crystal structure. The  $x=0.40$  Rietveld refinement revealed a very poor fit of the  $\{4\ 0\ 0\}_{pc}$ ,  $\{2\ 0\ 0\}_{pc}$   $\{2\ 2\ 2\}_{pc}$  reflections with the  $Amm2$  phase. Dramatic improvements in the fitting occur when considering the  $R3m$  Rhombohedral structure. The refined structural parameters obtained from Rietveld refinement for  $x=0.4$  are shown in Table SIV [13]. The Rietveld refinement on the XRD analysis reveals that BZT- $x$ BCT exhibits the single phase  $P4mm$  crystal structure in the regions,  $1.0 \leq x \leq 0.6$ , the co-existence of the  $P4mm + Amm2$  structure for the compositions range  $0.55 \leq x \leq 0.45$  and another single phase in the composition range  $0.3 \leq x \leq 0.4$  with  $R3m$  crystal structure. The phase coexistence model has been critically studied by plotting the variation of pseudo-cubic lattice parameters, unit cell volume and phase fraction obtained from Rietveld refinement, as shown in Fig. S1 (See Supplementary information) [13]. First, we have converted the orthorhombic lattice parameter ( $a$ ,  $b$ ,  $c$ ) into an equivalent perovskite pseudocubic lattice parameter using the following relation  $a_{pc}=a$ ,  $b_{pc}=b/\sqrt{2}$ ,  $c_{pc}=c/\sqrt{2}$  where  $a_{pc}$ ,  $b_{pc}$  and  $c_{pc}$  represents the lattice parameter for the strain free cubic lattice [64]. The obtained value of  $b_{pc}$  and  $c_{pc}$  are nearly same and both are larger than  $a_{pc}$ , so we introduce a term  $c_{avg} = (b_{pc} + c_{pc})/2$ .

For better representation, we have plotted the whole composition range into three different regions i.e. region (I)  $x=0.3-0.4$  (rhombohedral  $R3m$  Phase), region (II)  $x=0.45-0.55$  (coexistence of  $P4mm + Amm2$ ) phase and region (III)  $x=0.6-1.0$  (tetragonal  $P4mm$  phase) shown in Fig. S1 [13]. In region (I) i.e. at higher concentration of BZT, the rhombohedral ( $R3m$ ) lattice parameter ( $a_R$ ) is relatively high. The pseudocubic lattice parameter both in the regions I (corresponds to single phase rhombohedral structure with space group  $R3m$ ) and region III (corresponds to single phase tetragonal structure with space group  $P4mm$ ) decreases with the increase in BCT concentration. The decrease in the lattice parameter is due to the large ionic radius of  $Zr^{4+}$  as compared to  $Ti^{4+}$ . Similarly, the unit cell volume/formula

unit (f.u.) also decreases with the increase in the BCT concentrations both in the region I and region III. However, in the phase coexistence region (region II), the pseudocubic lattice parameter  $a_{pc}$  and  $c_{pc}$  corresponds to orthorhombic structure and the tetragonal lattice parameter  $a_T$  and  $c_T$  decreases slightly with increase in the BCT concentration up to  $x=0.5$  and these values increase with further increase in BCT concentrations. Similarly, the unit cell volume also shows a discontinuous change (change of slope) of its value around the phase coexistence region. For the composition  $x=0.3$  and  $0.4$ , the structure corresponds to purely rhombohedral ( $R3m$ ) (i.e., 100 % rhombohedral phase fraction). However, for  $0.45 \leq x \leq 0.55$  i.e. in the region (II) a phase coexistence of  $Amm2$  and  $P4mm$  is obtained. For  $x=0.45$ , the volume fraction of  $Amm2$  and  $P4mm$  is found to be 61% and 39%, respectively. With the increase in BCT concentration, the phase fraction of  $Amm2$  drops to 18% while that of  $P4mm$  rises to 82% for  $x=0.55$  and above that i.e.  $0.6 \leq x \leq 1.0$  it exhibits purely tetragonal ( $P4mm$ ) structure. The discontinuous changes in the unit cell volume and phase coexistence of two different crystallographic phases in the phase coexistence regions ( $0.45 \leq x \leq 0.55$ ), indicates the first order phase transitions from  $R3m$  (rhombohedral) to  $P4mm$  (tetragonal) through the  $Amm2 + P4mm$  phases [65].

## B. Raman Spectroscopy

Raman spectroscopy is a nondestructive probe of the structure of ferroelectric materials owing to its sensitivity to local symmetry. Raman scattering also provides information about local heterogeneities related to compositional and structural disorder because of the shorter coherence length and time scale of phonons. Therefore, the Raman spectra of the BZT- $x$ BCT system have been studied as a function of composition for realizing BCT doping effects to local heterogeneities structure of BZT- $x$ BCT ceramics. The reduced intensity,  $I^r(\omega)$ , corrected for the Bose-Einstein phonon population, was reckoned from Stokes components of observed Raman scattering intensity,  $I(\omega)$  as follows [66,67].

$$I^r(\omega) = \frac{I(\omega)}{\omega[n(\omega) + 1]} \quad (1)$$

Where,  $n(\omega) = \frac{1}{\exp\left(\frac{\hbar\omega}{k_B T}\right) - 1}$  represents the Bose-Einstein population factor.  $\hbar$  and  $k_B$

indicate Dirac and Boltzmann constants, respectively. To understand the BCT doping effects on BZT- $x$ BCT, all reduced Raman spectra in the frequency range of 50~100  $\text{cm}^{-1}$  were fitted by combining a Lorentzian central peak (CP), damped harmonic oscillator (DHO) model, and a Fano function as follows [66,67]:

$$I^r(\omega) = \frac{2A_{CP}}{\pi} \frac{\Gamma_{CP}}{4\omega^2 + \Gamma_{CP}^2} + \sum_i \frac{A_i \Gamma_i \omega_i^2}{(\omega^2 - \omega_i^2)^2 + \omega^2 \Gamma_i^2} + \frac{I_0(q + \varepsilon)^2}{(1 + \varepsilon)^2} \quad (2)$$

Where,  $A_{CP}$  and  $\Gamma_{CP}$  indicate the intensity and full width at half maximum (FWHM) of the CP, respectively, which is related to the relaxation process of precursor dynamics.  $A_i$ ,  $\omega_i$ , and  $\Gamma_i$ , represent intensity, frequency, and damping constant of the  $i^{\text{th}}$  optical Raman active mode, respectively. The  $I_0$  is the Fano resonance intensity,  $q$  reflects the asymmetry parameter representing the coupling strength between a continuum states and a discrete phonon,  $\varepsilon = 2(\omega - \omega_{A1(1TO)})/\Gamma_{A1(1TO)}$  denotes reduced energy, where  $\Gamma_{A1(1TO)}$  is the FWHM of the Fano resonance. The fitted Raman spectra using Eq. (2) are displayed in Fig. 3(b).

The composition dependent Raman spectra measured at room temperature of the BZT- $x$ BCT is shown in Fig. 3(a). The observed Raman spectra exhibit a similar profile of the pure BaTiO<sub>3</sub> (BT) [68]. Therefore, the effective vibrational modes of BZT- $x$ BCT ceramics are similar to that of pure BT. Pure BT is a typical ferroelectric material and it has tetragonal structure at room temperature. In the paraelectric cubic phase, the Raman modes of BT transform as the  $3T_{1u}+T_{2u}$  irreducible presentations of the  $Pm\bar{3}m$  symmetry. The  $F_{2u}$  mode is silent and  $F_{1u}$  modes are only infrared active. Therefore, the Raman activity is not allowed in the paraelectric phase with perfect cubic symmetry.

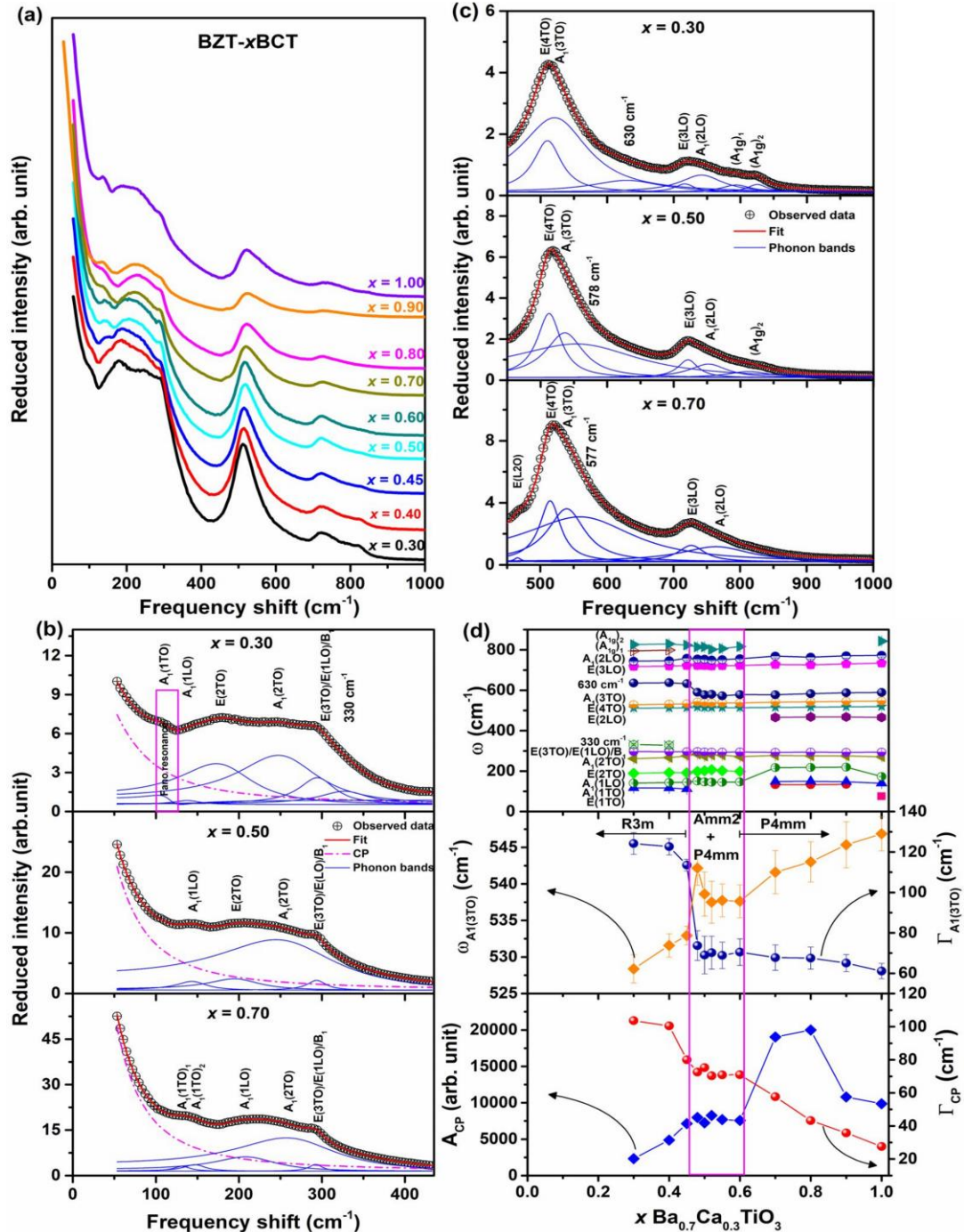


**FIG. 3.** (a) The composition dependent Raman spectra of BZT- $x$ BCT ceramics (b, c) Raman fitted spectra using Eq. (2) (d) Shows the frequency shift of Raman active modes (upper part), the frequency and FWHM of the  $A_1(3TO)$  mode (middle part), and the intensity and FWHM of the CP (lower part) of BZT- $x$ BCT ceramics as a function of composition.

A ferroelectric tetragonal phase with  $P4mm$  symmetry has  $3A_1$  and  $3E$  modes, which comes from infrared active  $F_{1u}$  modes and one silent ( $E+B_1$ ) mode arises from  $F_{2u}$  mode. Each of the  $A_1$  and  $E$  modes splits into transverse optic (TO) and longitudinal optic (LO) modes due to long-range electrostatic forces associated with lattice ionicity. The detailed mode symmetry assignments of  $BaTiO_3$  are reported elsewhere [69–71].

As can be seen in Figs. 3(b) and 3(c), the Raman spectrum in the frequency range of  $50\sim 1000\text{ cm}^{-1}$  of the BZT- $x$ BCT ( $x=0.30$ ) consist of mainly  $A_1(1TO)$  ( $\sim 117\text{ cm}^{-1}$ ),  $A_1(1LO)$  ( $\sim 140\text{ cm}^{-1}$ ),  $E(2TO)$  ( $\sim 189\text{ cm}^{-1}$ ),  $A_1(2TO)$  ( $\sim 261\text{ cm}^{-1}$ ),  $E(3TO)/E(1LO)/B_1$  ( $\sim 297\text{ cm}^{-1}$ ),  $E(4TO)$  ( $\sim 512\text{ cm}^{-1}$ ),  $A_1(3TO)$  ( $\sim 528\text{ cm}^{-1}$ ),  $E(3LO)$  ( $\sim 717\text{ cm}^{-1}$ ), and  $A_1(2LO)$  ( $\sim 744\text{ cm}^{-1}$ ). In BZT- $x$ BCT ( $x=0.3$ ), the broad peak at  $\sim 330\text{ cm}^{-1}$  may correspond to silent mode, which comes from higher order processes [72]. However, the weak mode near  $630\text{ cm}^{-1}$  (Fig. 3(c)) may be due to lattice disorder, which was attributed to mismatch of ionic radii at crystallographically equivalent sites [73]. At room temperature, the main spectral features observed in BZT- $x$ BCT ceramics are: Fano-like asymmetric  $A_1(1TO)$  mode, a symmetric  $A_1(1LO)$  mode, a symmetric broad  $E(2TO)$  mode, an asymmetric broad  $A_1(2TO)$  mode, a sharp  $E(3TO)/E(1LO)/B_1$  mode, symmetric intense  $E(4TO)$ ,  $A_1(3TO)$ , and  $E(3LO)$  modes, and a symmetric broad intense  $A_1(2LO)$  mode as shown in Figs. 3(b) and 3(c). The intense  $A_1(1TO)$ ,  $A_1(2TO)$ ,  $E(3TO)/E(1LO)/B_1$ ,  $E(4TO)/A_1(3TO)$ , and  $E(3LO)/A_1(2LO)$  modes correspond to the tetragonal phase of the pure BT [68]. An additional intense mode at  $\sim 189\text{ cm}^{-1}$  is observed in BZT- $x$ BCT ( $x=0.30$ ) besides phonon modes assigned to the tetragonal phase as shown in Figs. 3(a) and (b). The peak position of this mode shifted to the higher wave number up to  $\sim 202\text{ cm}^{-1}$  as the BCT composition increased from  $x=0.30$  to  $0.60$  in BZT- $x$ BCT ceramics. Xiao et al. [74] also found a Raman active mode at  $184\text{ cm}^{-1}$  in nanocrystalline BT ceramics, which was present in rhombohedral and orthorhombic phases. Hermet et al. [71] reported that the Raman active mode at  $\sim 205\text{ cm}^{-1}$  belongs to  $E(TO)$  symmetry of the rhombohedral phase of pure BT. Hence, the presence of Raman mode at  $\sim 189\text{ cm}^{-1}$  in this study is attributed to the  $E(TO)$  symmetry vibration, and the existence of  $E(2TO)$  mode is an indication of rhombohedral phase of the BZT- $x$ BCT ( $x=0.30$ ) ceramics. The rhombohedral phase with  $R3m$  symmetry of BZT- $x$ BCT ( $x=0.30$ ) ceramics is also confirmed by the Rietveld refinement of the XRD spectrum. It is significant that the  $A_1(1TO)$  mode slightly softens and completely disappears above  $x=0.45$  as shown in Figs. 3(a) and 3(b). The vanishing of  $A_1(1TO)$  mode and persisting of  $E(2TO)$  mode indicate the structural change in the material from rhombohedral to orthorhombic phase. In pure BT, the formation of peaks near  $117\text{ cm}^{-1}$  and  $261\text{ cm}^{-1}$  correspond to phonon vibrations of Ti-O bonds, whereas formation of peaks near  $515\text{ cm}^{-1}$  and  $717\text{ cm}^{-1}$  correspond to phonon vibrations of the Ba-O bonds. So, the frequency shifts of the  $A_1(1TO)$  mode towards low frequency region for BZT- $x$ BCT ( $0.30\leq x\leq 0.45$ ) may be due to dissimilar ions in the central octahedron of the perovskite structure. The BZT- $x$ BCT ceramic with  $x=0.30$ , (higher Zr content), compared to  $x=0.40$  and  $x=0.45$  experiences a downshift of the  $A_1(1TO)$  frequency which can be attributed to the variation of effective mass of the vibrational mode as Ti is smaller than Zr. So, the slight softening of the  $A_1(1TO)$  mode corresponds to replacement of Zr site with Ti. These results are similar to those observed previously in BZT- $x$ BCT ( $0.10\leq x\leq 0.20$ ) ceramics [22]. Note that the  $E(2TO)$  mode stiffens with increasing the BCT compositions and completely vanishes, while  $A_1(1LO)$  mode shows a clear anomaly above  $x=0.60$ , as shown in Fig. 3(d). Moreover, a new  $E(2LO)$  mode appears at  $\sim 466\text{ cm}^{-1}$  in the BZT- $x$ BCT ( $x=0.70$ ) ceramic (Fig. 3(c), lower part). The disappearance and appearance of Raman modes is a clear indication of structural transformation from orthorhombic to tetragonal phase above  $x=0.60$ . It is worth noting that  $A_1(1TO)$  mode splits in the tetragonal phase but not in the rhombohedral phase (Fig. 3(b)). This is may be due to the shift of polarization from  $[111]$  direction to  $[001]$  direction through  $[101]$  direction [75]. The Rietveld refinement of the XRD

spectra of BZT- $x$ BCT ( $0.60 \leq x \leq 1.0$ ) reveals the tetragonal phase with  $P4mm$  symmetry, while BZT- $x$ BCT ( $0.45 \leq x \leq 0.55$ ) shows the coexistence of orthorhombic ( $Amm2$ ) and tetragonal ( $P4mm$ ) phases. Singh et al. [76] reported the coexistence of phases in BZT- $x$ BCT ( $x=0.50$ ) by observing the hysteresis behaviour of the  $A_1(3TO)$  mode. Therefore, we have also studied the  $A_1(3TO)$  mode as a function of composition in order to have a better understanding of the phase transitions of BZT- $x$ BCT ceramics. The composition dependent frequency and FWHM of the  $A_1(3TO)$  mode is shown in the middle part of Fig. 3(d). It is apparent that the FWHM of the  $A_1(3TO)$  mode decreases, while the frequency shows significant stiffening and a discontinuity at above  $x=0.45$ , reflecting the structural transformation from the rhombohedral phase. Note that the frequency and FWHM of the  $A_1(3TO)$  mode are almost constant in the range of  $0.45 < x \leq 0.60$ . The frequency increases and FWHM decreases continuously with increasing BCT compositions above  $x=0.60$ . The constant frequency and damping of the  $A_1(3TO)$  may due to the coexistence of phases in the range of  $0.45 < x \leq 0.60$ . Hence, the anomalous change of the  $A_1(3TO)$  mode at  $x=0.45$  corresponds to structural transformation from pure rhombohedral to (orthorhombic + tetragonal) phase, and another anomaly at  $x=0.60$  corresponds to (orthorhombic + tetragonal) to a pure tetragonal phase transition of BZT- $x$ BCT ceramics. Since the formation of peaks  $\sim 515 \text{ cm}^{-1}$  correspond to phonon vibrations of the Ba-O bonds, so the stiffening of the  $A_1(3TO)$  is likely due to replacement of Ba site with Ca as the atomic number of Ba is higher than that of Ca. The high frequency region around  $825 \text{ cm}^{-1}$  shows an  $A_{1g}$  octahedral breathing mode. The symmetric  $A_{1g}$  octahedral breathing mode occurs in this region for simple perovskite, which is Raman inactive and does not result in a change in polarization [77]. The  $A_{1g}$  mode (upper part of Fig. 3(c)) becomes Raman active when dissimilar ions in the center of the octahedra creates asymmetry in the breathing-like mode [22]. The breathing ( $A_{1g}$ )<sub>1</sub> mode merges into the ( $A_{1g}$ )<sub>2</sub> mode at  $x=0.45$ , and the breathing ( $A_{1g}$ )<sub>2</sub> mode completely vanished above  $x=0.60$  as shown upper part of Fig. 3(d). The merging and disappearing  $A_{1g}$  modes can be an indication of structural transformation as well.

In BZT- $x$ BCT ( $x=0.30$ ) ceramics, the Raman spectrum is fitted using Fano function at around  $117 \text{ cm}^{-1}$  as shown in Fig. 3(b). The Fano resonance phenomenon stems from the interaction between a discrete state and continuum states and has an asymmetry of the spectral line shape [78]. However, the physical origin of the Fano resonance in BZT- $x$ BCT at  $\sim 117 \text{ cm}^{-1}$  still remains unclear. The Fano resonance  $\sim 175 \text{ cm}^{-1}$  in pure BT single crystal was attributed to the interference effect ensuing from the coupling between two acoustical phonon states and a single phonon state through the anharmonic terms in the potential function studied by Rousseau and Porto [79]. The Fano-like interference  $\sim 175 \text{ cm}^{-1}$  in pure BT crystals may be due to the anharmonic coupling of the lowest frequency TO phonon with the higher frequency TO phonon via acoustic phonons reported by Pinczuk et al. as well [80]. In BZT- $x$ BCT, the acoustic phonon mode is not observed in the present investigation. Hence, the coupling between the  $A_1(1TO)$  mode and acoustic phonon modes cannot be the origin of the Fano resonance in BZT- $x$ BCT ceramics. The possible origin of Fano resonance in BZT- $x$ BCT at  $\sim 117 \text{ cm}^{-1}$  may be due to the coupling between  $A_1(1TO)$  and  $A_1(2TO)$  modes [22]. Due to the vanishing of the  $A_1(1TO)$  mode, the Fano resonance also disappears in BZT- $x$ BCT at above  $x=0.45$  as shown in Fig. 3(a) and 3(b). However, the Fano-like asymmetric line shape appears in BZT- $x$ BCT ( $x=1.0$ , BCT) near the  $A_1(1TO)$  mode (Fig. 3(a)). In BCT, we failed to fit the Raman spectrum assuming Fano function at  $\sim 140 \text{ cm}^{-1}$  [ $A_1(1TO)$  mode], while the spectrum was well fitted considering the Fano function at  $\sim 173 \text{ cm}^{-1}$  [ $A_1(1LO)$  mode] in the present study (See Fig. S2 in Supplementary information) [13], and this fact rules out the coupling between  $A_1(1TO)$  and  $A_1(2TO)$ . It is found that the Fano resonance near  $117 \text{ cm}^{-1}$  of the BZT- $x$ BCT ( $x=0.3$ ) is well fitted with negative value of  $q \sim -0.978 \pm 0.24$ , and the Fano resonance near  $173 \text{ cm}^{-1}$  of the BCT is fitted with the positive value of  $q \sim$

1.759±0.22. The physical origin of Fano resonance in Li-doped  $\text{KTa}_{1-x}\text{Nb}_x\text{O}_3$  single crystal at  $\sim 196 \text{ cm}^{-1}$  has been attributed to the coupling between the broad CP, which gives rise to polarization fluctuations of local polar clusters called polar nano regions (PNRs), and the  $E(2\text{TO})$  mode by observing the positive  $q$  value [66,67]. The prominent CP of BZT- $x$ BCT ( $x=1.0$ ) ceramics has been observed as shown in Figs. 3(a) and 3(b). By Brillouin scattering, Ko et al. [81] reported the CP of pure BT, which was attributed to PNRs due to off-center displacements of Ti at B-site with hopping motion along equivalent [111] directions [82]. Banerjee et al. [83] also studied the Fano resonance with the polarization fluctuations in PNR continua and observed a positive value of  $q$ . So, coupling between the broad CP and the  $A_1(1\text{LO})$  mode may be the origin of Fano resonance of the BCT ceramic. Recently, Pradhan et al. [84] reported the physical origin of Fano resonance of Co-doped BT is the coupling between a discrete  $A_1(\text{LO}_1)$  phonon around  $173 \text{ cm}^{-1}$  and the broad CP, due to rapid polarization fluctuations in PNRs.

We have studied the composition dependence of the CP behavior in order to have a better understanding of the effects of BCT composition on local heterogeneities in BZT- $x$ BCT ceramics. The soft mode expresses a common property of either a ceramic or a crystal undergoing the displacive phase transition, and the CP is the general property of the order-disorder phase transition of ferroelectric materials. We do not observe the low frequency  $E(1\text{TO})$  phonon mode in the BZT- $x$ BCT ( $0.30 \leq x \leq 0.9$ ) in this study. However, we observed a phonon mode at  $74 \text{ cm}^{-1}$  [ $E(1\text{TO})$ ] in BZT- $x$ BCT ( $x=1.0$ ) as shown in the supplementary information. The  $E(1\text{TO})$  mode was also found in the tetragonal phase of pure BT [68]. Due to lack of temperature dependent Raman scattering results, it is difficult to comment on the soft-mode behaviour of the  $E(1\text{TO})$  mode. Therefore, the existence of prominent CP is a clear indication of the order-disorder nature of ferroelectric phase transition of BZT- $x$ BCT ceramics [66,67,81]. It is well known that the fluctuating PNRs begin to appear at the so-called Burns temperature ( $T_B$ ) in the paraelectric cubic phase [85], whereas these dynamic PNRs become static at an intermediate temperature ( $T^*$ ) [66,67]. Owing to the freezing of local polarization, these static PNRs becomes randomly oriented nano-domain states and transform into macro-domain states in the ferroelectric phase [49,86]. It is seen from the lower part of Fig. 3(d), that the FWHM of the CP, which is related to the relaxation process of precursor dynamics [66,67,81], decreases with increasing BCT composition of BZT- $x$ BCT ceramics. This result suggests that the correlation among nano-domain states may be strengthened with increasing BCT composition below and above the MPB region ( $0.45 < x \leq 0.60$ ) due to the increase of size and/or number density of randomly oriented nano-domain states. This enhances the relaxation process of domain wall motion and results in an increase of the CP intensity. However, the intensity and FWHM of the CP is almost constant in the MPB region, in which BZT- $x$ BCT belongs to (orthorhombic + tetragonal) phases. Owing to the coexistence of phases, the correlation among nano-domain states may weaken and/or be broken giving rise to the almost constant fluctuations of domain wall motion and results in constant CP intensity in the MPB. The motion of ferroelectric domain walls of  $\text{BaTiO}_3$  was observed by confocal Raman spectroscopy as well [87].

### C. Theoretical Results

In an effort to further elucidate the atomistic origins of the observed phase competition and functional properties of lead-free BZT- $x$ BCT ceramics as a function of composition, we performed first-principles calculations based on density functional theory. Figure 4(a) illustrates the unit cell and Fig. 4(b) shows the zero-temperature DFT energy estimated for the four selected BZT- $x$ BCT polymorphs (i.e., tetragonal  $P4mm$  -T-, cubic  $Pm\bar{3}m$  -C-, rhombohedral  $R3m$  -R-, and orthorhombic  $Amm2$  -O-) considering four different compositions.

In accordance with the experiments, we find a very strong phase competition between the three polar polymorphs T, R and O for compositions around  $x=0.50$  (the two simulated composition systems  $x=1.00$  and  $0.00$  also reproduce the stable phases observed in the XRD and Raman experiments (Fig. 4(b)).

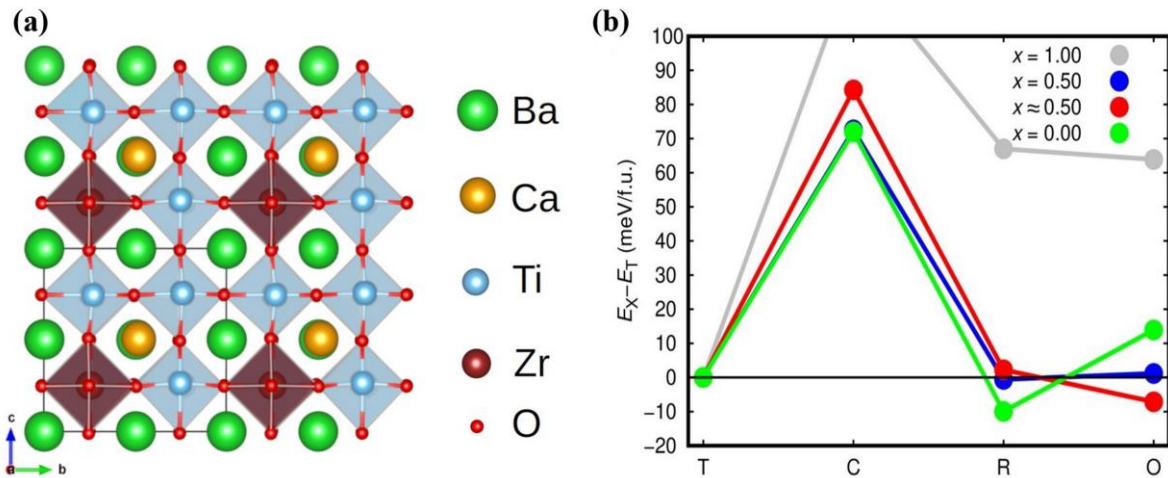


**FIG. 4.** First-principles characterization of lead-free BZT- $x$ BCT ceramics based on density functional theory calculations. (a) Sketch of the simulation cell employed in the first-principles calculations (black solid lines). (b) Energy difference results as obtained for the tetragonal ( $P4mm$ , “T”), cubic ( $Pm3m$ , “C”), orthorhombic ( $Amm2$ , “O”) and rhombohedral ( $R3m$ , “R”) phases lead-free BZT-BCT ceramics as a function of composition.

Specifically, at  $x=0.50$  the energy differences between the three polar phases is of the order of 1 meV per f.u. or below and we predict the R phase to be the ground-state structure (note that thermal effects are systematically disregarded in our first-principles calculations). As the content of BCT is marginally reduced, the O polymorph clearly becomes energetically more favorable than the others. For instance, at  $x \approx 0.50$  the energy difference between the O and T polymorphs is 7 meV per f.u. and between O and R is 9 meV per f.u.. Thus, the DFT calculations are in good agreement with the observation that upon varying the ceramics composition from  $x=0.50$  to  $0.45$  the fraction of O phase increases considerably.

#### D. Surface Morphology

Figures S3(a)-S3(c) (See Supplementary information [13]) shows the scanning electron micrographs (SEM) of BZT- $x$ BCT for  $x=0.4, 0.5, 0.6$  as representative images (other compositions are not shown here). The micrographs show highly dense microstructure in which the polyhedral grains are well developed and separated by grain boundaries. The grains are inhomogeneously distributed throughout the microstructure with a few scattered pores. The surface microstructure of BZT- $x$ BCT samples is strongly dependent on the composition. The average grain size was calculated using Image J software. The grain size of  $x=0.3$  is found to be  $1.5 \mu\text{m}$  with very fine and well-connected grains. The grain size increases with an increase in BCT concentration and for pure BCT the grain size found to be around  $13 \mu\text{m}$  as shown in the Fig. S3(d) [13]. This implies that BCT promotes the grain growth of the material. The elemental composition in our system is further investigated via energy dispersive X-ray spectroscopy (EDX). EDX spectra show the presence of all the cationic elements in the compounds with proper stoichiometry within an error limit of  $\pm 10\%$  (provided in Supplementary information Fig. S4) [13].

#### E. Electrical Properties

## 1. Dielectric Properties

To study the phase transition behaviour in BZT- $x$ BCT ceramics, temperature dependent dielectric properties i.e., dielectric permittivity ( $\epsilon_r$ ) and dielectric loss ( $\tan\delta$ ) for different frequencies were investigated. The temperature dependence dielectric permittivity and dielectric loss at various frequencies for BZT- $x$ BCT with  $x=1.0, 0.55, 0.5, 0.4$  is shown in Figs. 5(a)-5(d) as representative plots. The dielectric permittivity decreases with increasing frequency for all compositions irrespective of temperature suggesting the typical behaviour of polar dielectric materials as shown in Fig. 5. For all the compositions, the dielectric permittivity increases with increase in the temperature at all frequencies up to the ferroelectric phase transition temperature. With further increase in temperature the dielectric permittivity values decrease. For pure BCT ( $x=1.0$ ), the ferroelectric to paraelectric phase transition is a sharp phase transition with a transition temperature of 120 °C as observed in Fig. 5(a). With decreasing BCT concentration, the phase transition becomes more diffuse, i.e, broadening of the phase transition around  $T_m$ . For  $x=0.3$  and 0.4, a highly diffuse phase transition behaviour is observed. This result is consistent with previous reports of the PMN-PT system [88]. Similarly, from the dielectric loss plots a single sharp anomaly is observed for pure BCT and the peak becomes broadened at higher BZT concentrations. Diffuse phase transitions in a material are generally characterised by certain features such as (i) the broadness of dielectric permittivity ( $\epsilon_r$ ) versus temperature curve (ii) a relatively large difference in the temperature corresponding to the maximum dielectric permittivity ( $\epsilon_r$ ) and dielectric loss ( $\tan\delta$ ) of the dielectric spectra (iii) frequency dispersion of both  $\epsilon_r$  and  $\tan\delta$  in the transition region suggesting a frequency dependent temperature of maximum dielectric permittivity (iv) a deviation from the Curie Weiss law in the vicinity of maximum dielectric temperature [89].

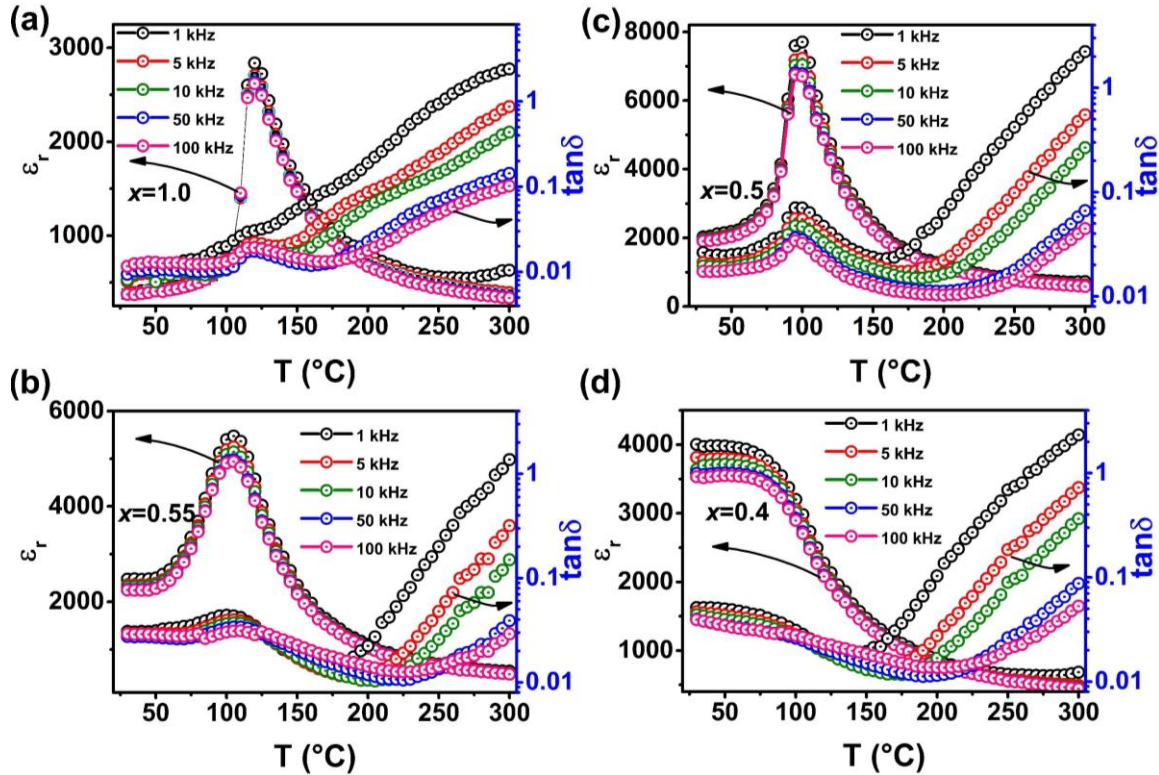


**FIG. 5.** Temperature ( $T$ ) dependence dielectric permittivity and dielectric loss of BZT- $x$ BCT with the composition (a)  $x= 1.0$  (b)  $x=0.55$  (c)  $x=0.5$  (d)  $x=0.4$  at some selected frequency.

The broad dielectric curve at higher BZT content is due to the larger ionic radius and lower polarization value of  $Zr^{4+}$  as compare to  $Ti^{4+}$  [27]. The observed diffuse phase transition is due to the cation disorder i.e., compositional fluctuation of the different polar micro regions where different ions ( $Ba^{2+}$ ,  $Ca^{2+}$ ,  $Ti^{4+}$ ,  $Zr^{4+}$ ) occupy at the same crystallographic sites in the  $ABO_3$  perovskite.

Further to quantify the diffuseness, the modified Curie Weiss equation is used to fit the temperature dependent dielectric permittivity data. The modified Curie Weiss can be expressed as  $\frac{1}{\epsilon_r} - \frac{1}{\epsilon_m} = \frac{(T - T_m)^\gamma}{C}$  where  $C = 2\epsilon_m\delta^\gamma$ ,  $\epsilon_m$  is the dielectric permittivity at  $T_m$ ,  $T_m$

represents the temperature at which maximum dielectric permittivity is observed,  $\gamma$  the degree of relaxation/diffuseness,  $\delta$  the diffuseness parameter and  $C$  the Curie Weiss constant. The value of  $\gamma$  is found to be 1 for normal ferroelectric and  $\sim 2$  for highly diffuse ferroelectric phase transitions [90]. In order to verify the modified Curie Weiss law, the temperature dependent dielectric permittivity data has been plotted in log-log plot in the paraelectric region (just above the  $T_m$ ) as shown in the inset Fig. 6(c) for  $x=0.5$ . The linear fit of this plot suggesting the verification of modified Curie Weiss equation. The slope of the curve gives the value of  $\gamma$  and from the intercept of this curve,  $\delta$  can be calculated.

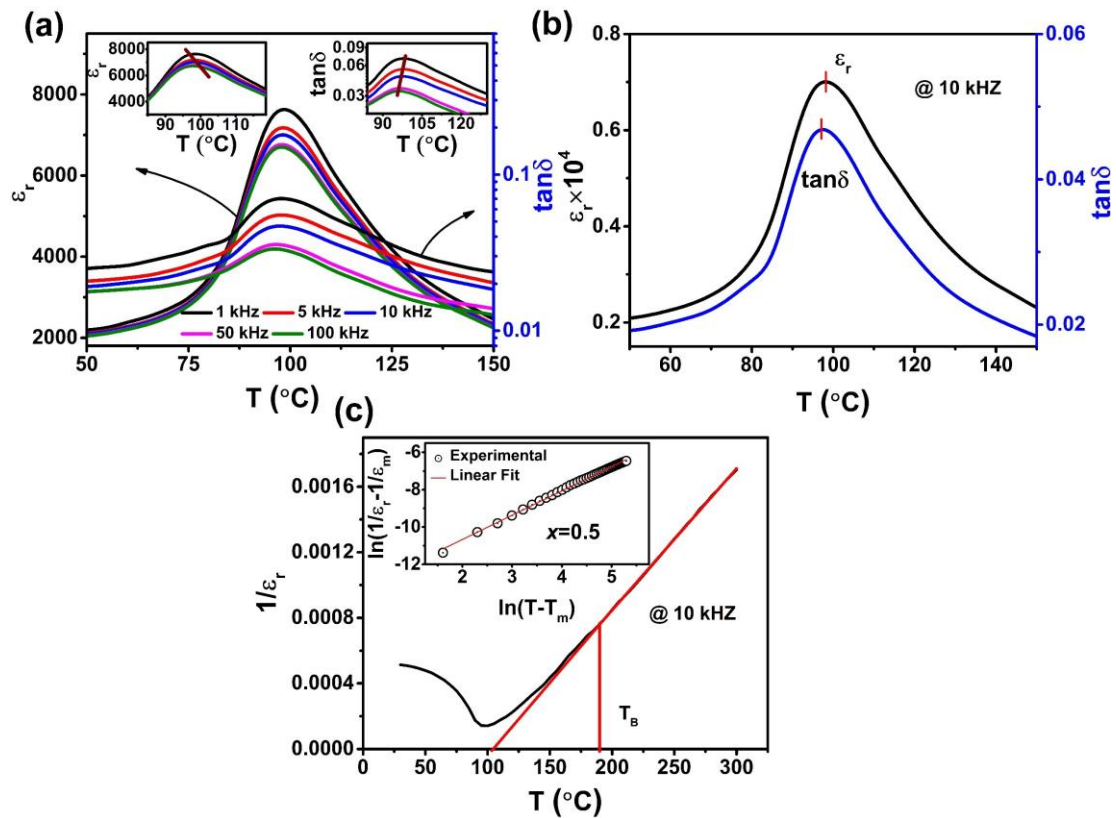


**FIG. 6.** (a) Temperature ( $T$ ) dependence of dielectric permittivity and dielectric loss at different frequencies for the composition  $x=0.5$ . The inset of (a) shows the magnified plot of temperature dependent dielectric permittivity and dielectric loss to reveal the frequency dependence of the peak temperature. (b) Magnified plot of dielectric permittivity and dielectric loss to reveal the difference in the corresponding peak temperature at a given frequency of 10 kHz for  $x=0.5$ . (c) Variation of  $1/\epsilon_r$  as a function of temperature at 10 kHz

with  $x=0.5$ ,  $T_B$  corresponds to Burn temperature. Inset of (c) shows a Modified Curie Weiss law fit ( $\ln(1/\epsilon_r - 1/\epsilon_m)$  vs.  $\ln(T - T_m)$ ) of temperature dependent dielectric permittivity

For all the compositions, the values of  $\gamma$  and  $\delta$  are plotted as a function of composition as shown in the Fig. 7. The  $\gamma$  value is found to be 1.1 for pure BCT, however with decreasing BCT concentration this value increases to 1.8 for  $x=0.4$  (shown in Fig. 7). There is a discontinuous change in the  $\gamma$  value with the composition around the phase coexistence region. This confirms the material exhibits a strong diffuse phase transition at higher BZT concentration [89]. For  $x=0.5$ , the fitted parameters are found to be  $\gamma = 1.47$  and  $\delta = 23.6$ , which is close to the previously reported value [34]. The ferroelectric transition temperature  $T_m$  and  $\epsilon_m$  (around  $T_m$ ) are strongly dependent on the composition as shown in Fig. 7. It is observed that  $\epsilon_m$  increases with the increasing BCT composition up to  $x=0.5$ ; increasing BCT beyond  $x=0.5$ ,  $\epsilon_m$  decreases. Such a large dielectric response at  $x=0.5$  is coincident with the MPB ( $Amm2 + P4mm$ ) region. The observed phase transition temperatures match well with previously reported values [91]. We have also calculated the tolerance factor ( $t$ ) for the entire composition range. The tolerance factor decreases with increasing BCT concentrations where the higher transition temperature correlates with lower tolerance factors as predicted by R. E. Eitel et al. [92].

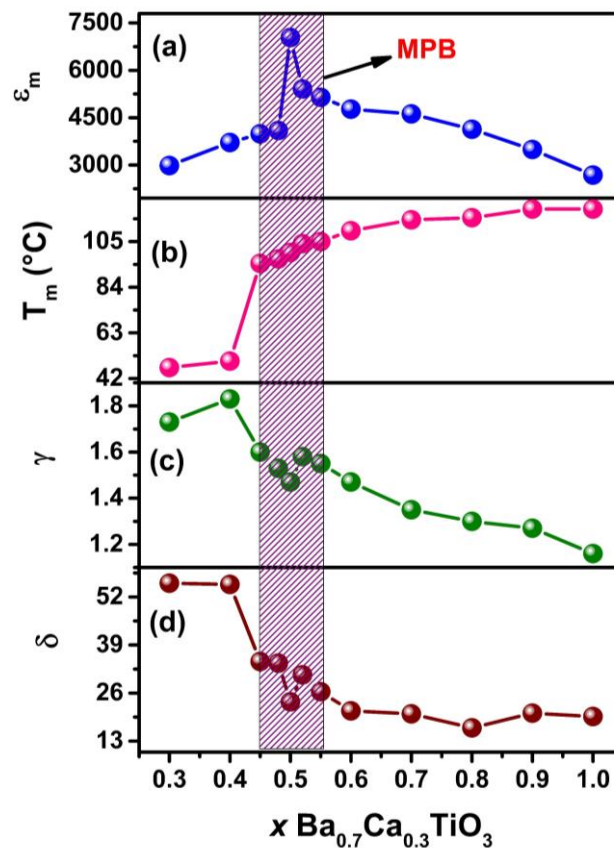


**FIG. 7.** Variation of (a) Dielectric permittivity ( $\epsilon_m$ ) around transition temperature ( $T_m$ ) (b) Transition temperature ( $T_m$ ) (c) Degree of diffuseness ( $\gamma$ ) (d) Diffuseness parameter ( $\delta$ ) with composition ( $x$ ) of BZT- $x$ BCT in the composition range of  $0.3 \leq x \leq 1.0$ .

### *i. Evidence of Relaxor Ferroelectricity*

Figure 6(a) depicts the temperature dependent dielectric permittivity and loss tangent data for BZT- $x$ BCT ( $x=0.5$ ) at different frequencies in the temperature range of 50-150 °C. Similarly,

the temperature dependent dielectric properties are also observed for compositions  $x=0.45, 0.48, 0.52, 0.55$  (shown in Figs. S5-S8 in Supplementary information) [13]. A single broad dielectric anomaly in the temperature dependent dielectric permittivity is observed around  $100\text{ }^{\circ}\text{C}$  ( $T_m$ ) for  $x=0.5$ . The dispersion in the dielectric permittivity is more pronounced around  $T_m$ . However, with the increasing temperature the degree of dispersion decreases and vanishes above  $190\text{ }^{\circ}\text{C}$ . This type of behaviour suggests the formation of PNRs, which is a typical characteristic of relaxor ferroelectricity [34,93]. The dielectric permittivity peak slightly shifts towards higher temperature with increasing frequency around  $T_m$ , which is clearly visible in the inset of Fig. 6(a). On the other hand, the opposite trend is observed for the loss tangent, i.e., upon increasing frequency the loss peak shifts towards lower temperatures (as observed in inset of Fig. 6(a)). To further illustrate this point, we have plotted the dielectric permittivity and loss at a frequency of  $10\text{ kHz}$  around the phase transition region as shown in Fig. 6(b). There is a small difference in the transition temperature for the permittivity and loss peak, i.e., the dielectric permittivity peak occurs at a higher temperature relative to the loss peak [34,93]. This type of behaviour confirms the relaxor nature of the analysed material and our observation is consistent with a previous report [34]. Similar type of behaviour is also observed for other MPB compositions, i.e.,  $x=0.45, 0.48, 0.52, 0.55$ . (See Figs. S5-S8 in Supplementary information) [13].

The temperature below which the frequency dependent dielectric permittivity curve branches off can be considered as the Burns temperature ( $T_B$ ). Furthermore, the temperature around which the deviation from the Curie Weiss behaviour is observed can be regarded as  $T_B$ , as it has been previously justified in the literature [34]. The plot of  $1/\epsilon_r$  expressed as a function of temperature at  $10\text{ kHz}$  is shown in Fig. 6(c) and used to determine  $T_B$ . A significant departure from the Curie Weiss behaviour is observed below  $190\text{ }^{\circ}\text{C}$ , suggesting this temperature to be  $T_B$  (below which the dynamic polar regions are expected to appear) [64,94]. Upon cooling, the polar nanoregions (PNR) start to developed inside the crystal, instead of micrometer scale ferroelectric domains with randomly orientated dipole moments. Note that  $T_B$  is well above  $T_m$  [95]. These PNRs are not static in nature at  $T_B$ , with the dipole moment thermally fluctuating between equivalent polarization directions [96]. All of the above point to the relaxor behaviour for the composition  $x=0.5$ . This type of relaxor behaviour is present mainly for  $x=0.48$  and  $0.52$  in the MPB compositions. However, around  $T_m$ , a broad dielectric peak and weak dispersion behaviour is observed for the MPB compositions at  $x=0.45$  and  $0.55$ , but  $\epsilon_r$  and  $\tan\delta$  peaks occur at nearly the same temperature. This suggests a weak relaxor like behaviour for these compositions (See Figs. S5-S8 in Supplementary information) [13]. In the rhombohedral phase, the phase transition is more diffusive and in the tetragonal phase region the phase transition is sharp. However, around the MPB compositions weak relaxor-like behaviour is clearly visible.

## 2. *Ferroelectric Properties*

To confirm the ferroelectric behaviour, room temperature ferroelectric (P-E) hysteresis loops for BZT- $x$ BCT were recorded in the composition range of  $0.3 \leq x \leq 1.0$ . Figures 8(a)-8(c) shows the hysteresis loop of poled samples at a testing frequency of  $10\text{ Hz}$ . The shape of the P-E loop changes with changing BZT- $x$ BCT compositions as shown in the Figs. 8(a)-8(c). Higher BZT concentrations ( $x=0.3-0.4$ ) exhibit a narrow hysteresis loop suggesting the samples are soft in nature with respect to applied electric field [97,98]. This narrow P-E loop can be attributed to the combination of macro and micro polar regions, and results in an enhanced diffused phase transition (DPT) effect [99]. This behaviour is consistent with the temperature dependent dielectric results. However, with increasing BCT concentration, the area of the hysteresis loop increases, which implies more energy required to reverse the dipole. The P-E

loop exhibits a nonlinear, well-defined and saturated loop for all the compositions. The ferroelectric parameters such as remnant polarization  $2P_r = P_r^{+0} - P_r^{-0}$  and coercive field  $E_c = (E_c^{+0} - E_c^{-0})/2$  is calculated from the P-E loops. The switchable polarisation i.e.  $2P_r$  and the coercive field ( $E_c$ ) are plotted as a function of  $x$  in Fig. 8(d). Composition  $x=0.3$ , exhibits a low remnant polarisation ( $2P_r$ ) value of  $5.38 \mu\text{C}/\text{cm}^2$  with a low coercive field of  $1.59 \text{ kV}/\text{cm}$ . The  $2P_r$  increases with increasing BCT concentration and the maximum value is found to be  $19.47 \mu\text{C}/\text{cm}^2$  for  $x=0.5$ .

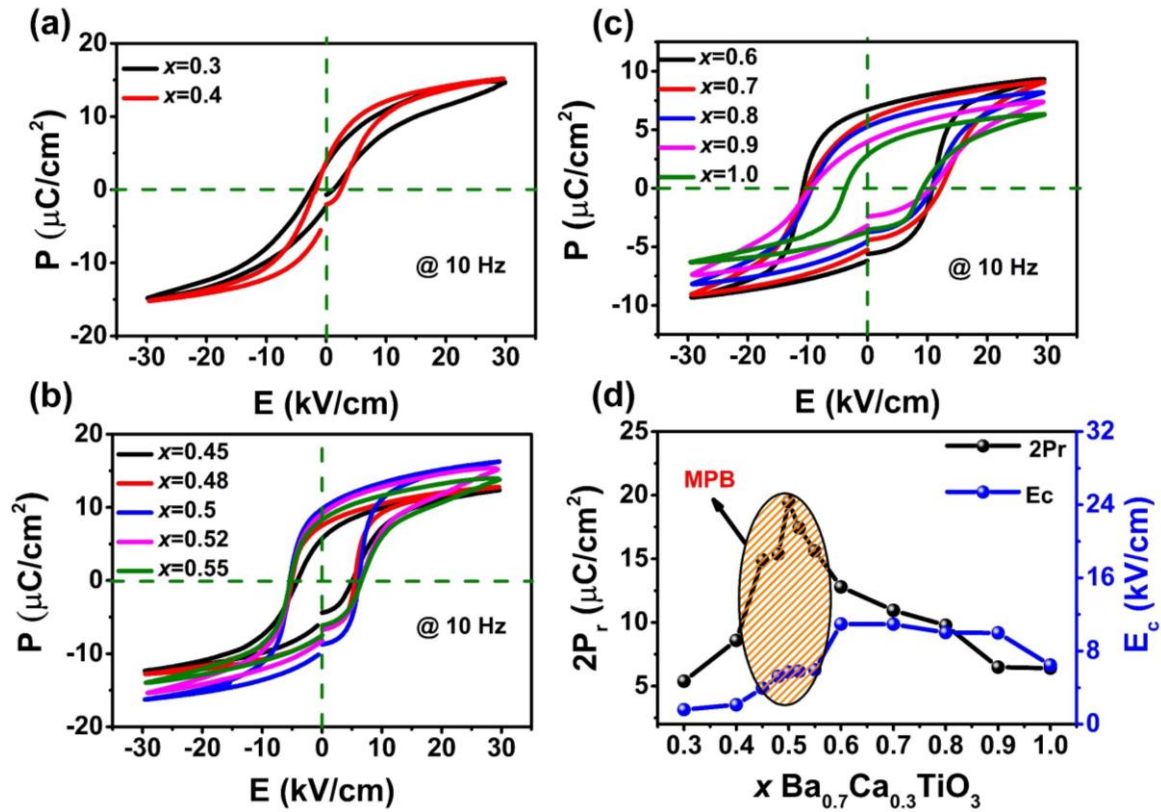


**FIG. 8.** Ferroelectric hysteresis (P-E) loop of poled sample of BZT- $x$ BCT ceramic for (a)  $x=0.3-0.4$  (b)  $x=0.45-0.55$  (c)  $x=0.6-1.0$  (d) Variation of  $2P_r$ ,  $E_c$  for BZT- $x$ BCT with the composition range of  $0.3 \leq x \leq 1.0$ .

At higher BCT composition,  $2P_r$  value decreases up to  $x=1.0$ . The rate of increasing/decreasing polarization value is greatest in the phase coexistence regions i.e., around MPB compositions. However, the coercive field ( $E_c$ ) increases with increasing BCT concentrations up to  $x=0.6$  and above this composition, the  $E_c$  value saturates. The value of coercive field for the rhombohedral phase ( $x=0.3$  and  $0.4$ ) is much lower than the value of the tetragonal phase ( $0.6 \leq x \leq 1.0$ ), which is consistent with a previous report [100]. The lower value of both the  $2P_r$  and  $E_c$  value in the rhombohedral ( $0.3 \leq x \leq 0.4$ ) phase implies a disturbance of the long-range ferroelectric ordering due to the restriction in ionic displacement (decrease in the rattling space available for the movement of B-site cations) because of the higher ionic radii of  $\text{Zr}^{4+}$  compared to  $\text{Ti}^{4+}$  [97]. The lower value of both the  $2P_r$  and  $E_c$  value can also be due to the uniform grain size and decrease in the tetragonal phase fraction, which is consistent with both XRD and microscopy results. The lower value of  $2P_r$  in the tetragonal phase region, is due the decrease in the unit cell volume with increasing BCT concentration. The higher  $E_c$  value in the tetragonal phase suggests the domain wall pinning phenomena. The higher value of  $2P_r$  with a low value of coercive field

as observed in the range of  $0.45 \leq x \leq 0.55$  is consistent with a MPB region (shown in Fig. 8(d)) as shown in previous theoretical reports [10–12].

### 3. Piezoelectric Properties

The variation of piezoelectric coefficient ( $d_{33}$ ) of BZT- $x$ BCT ceramics as a function of BCT concentration at room temperature is shown in Fig. 9. The  $d_{33}$  value is found to be 29 pC/N for  $x=0.3$ . With increasing BCT content, the  $d_{33}$  value increases and reaches to a maximum value for  $x=0.5$ , then decreases with a further increase in BCT concentration. The rate of change in the  $d_{33}$  value is higher in the composition range of  $0.45 \leq x \leq 0.55$  (in the phase coexistence MPB region) with the maximum value of  $d_{33}$  found to be 320 pC/N for  $x=0.5$ . The variation of  $d_{33}$  is similar to the variation of  $\epsilon_r$  and  $P_r$  with composition and the maximum value of these physical properties all correlate to the  $x=0.5$  composition. The reason for the enhancement of  $d_{33}$  around the MPB is discussed below.

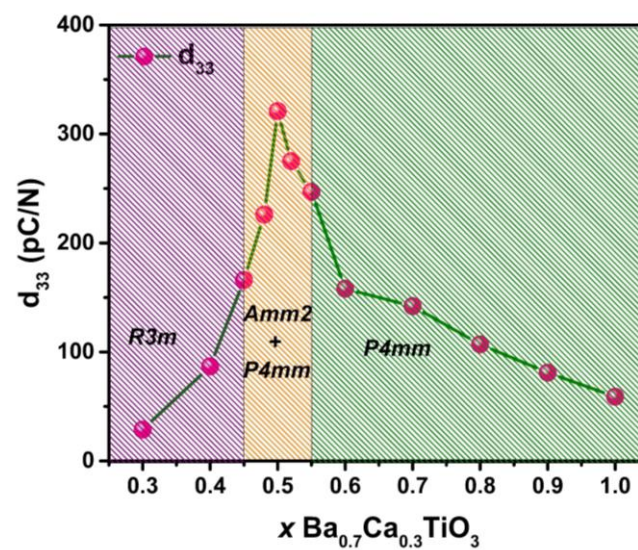


**FIG. 9.** Variation of  $d_{33}$  for BZT- $x$ BCT with in the composition range of  $0.3 \leq x \leq 1.0$ .

## IV. DISCUSSION

The observation of the composition driven structural phase transition around the MPB region of perovskite based solid solutions is of great practical interest as well from the fundamental physics point of view [101]. The origin of the MPB composition in ferroelectric solid solutions has been studied based on the Landau free energy functions and reported that the composition in the vicinity of MPB region shows large dielectric susceptibility and piezoelectric coefficients with extremely small coercive field and stiffness constant [10–12]. First principle and phenomenological investigations suggest that the anisotropic flattening of the free energy profile gives rise to the polarization rotation with a low energy pathway around the MPB compositions and thus the principal mechanism for the enhanced piezoelectric properties [102]. The piezoelectric coefficient ‘ $d$ ’ of the ferroelectric oxides having a perovskite structure can be represented by  $d=2P_sQ\epsilon$ , where  $P_s$ = spontaneous polarization,  $Q$ = electro-strictive coefficient, and  $\epsilon$ = dielectric permittivity [103]. Using the phenomenological thermodynamic theory, the dielectric permittivity (i.e., dielectric susceptibility ( $\chi$ )~ dielectric permittivity for ferroelectric systems) is represented by the curvature of the free energy density profile with respect to polarization (i.e.,  $\frac{\partial^2 G}{\partial p^2} \propto \frac{1}{\chi}$ ) [7,53,102,103]. Small curvature, i.e., flat free energy profile, produces a higher

value of  $\epsilon$ , which is ultimately responsible for the enhancement of the piezoelectric coefficient. It has been well accepted that the free energy profile flattens around MPB compositions of the ferroelectric solid solutions, which is responsible for the enhancement of  $\epsilon$  as well as  $d$ . As the compositional induced structural phase transition is a first order phase transition (this signature has been reflected in terms of the coexistence of T and O crystallographic phases in our case), an ideally flat free energy profile (i.e.,  $\frac{\partial^2 G}{\partial p^2}$  tends to zero)

cannot be achieved. However, the free energy profile can further flatten by inducing a local structural heterogeneity to manipulate the interfacial energy i.e., electrostatic and elastic energy associated with the interface [103,104]. Based on the computational and experimental investigation, M. Acosta et al. [52] suggested that the enhanced piezoelectric properties in BZT- $x$ BCT system around the MPB region cannot be fully reconciled by the reduction in the anisotropic energy or flattening of the free energy. They further suggest that the reduction of the anisotropic energy is the necessary condition for enhanced piezoelectric properties but not the sufficient condition for maximizing the piezoelectric properties, which was further supported by Cordero et al. [52,105]. The optimum/sufficient condition is the greatest elastic softening and retention of high spontaneous/remnant polarization [105].

The symmetry allowed polarization rotation phenomena can be used to explain the enhancement of the piezoelectric properties due to flattening of anisotropic free energy in BZT- $x$ BCT system around the MPB due to composition induced structural phase transitions [103,106]. At  $x=1.0$ , BCT belongs to tetragonal ( $P4mm$ ) crystal structure and  $x=0.3$  belongs to rhombohedral ( $R3m$ ) crystal structure. The transition from  $P4mm$  to  $R3m$  is not allowed by the symmetry considerations, however it can be mediated through a low symmetry phase [20,52,106]. The tetragonal strain is dominant over the rhombohedral strain, which induces an orthorhombic instability in the lattice and serves as structural bridge (where polarization rotation occurs among the different polarization states) connecting between  $R3m$  and  $P4mm$  phases in the MPB [27]. As the BT based system is similar to the PZN- $x$ PT system, the low symmetry orthorhombic ( $Amm2$ ) phase can be expected [103]. The BZT- $x$ BCT system undergoes a phase transition from the rhombohedral ( $R3m$ ) to tetragonal ( $P4mm$ ) phase through the coexistence of tetragonal ( $P4mm$ ) + orthorhombic ( $Amm2$ ) in the MPB region as confirmed from the XRD and Raman data. The polarization vector rotates from the rhombohedral [111] direction ( $R3m$ ) to the tetragonal [001] direction ( $P4mm$ ), through the [101] orthorhombic direction ( $Amm2$ ). The polarization rotation behaviour has been described in supplementary materials Fig. S9 (See Supplementary information [13]; also see Refs. [107–110] therein). The orthorhombic phase ( $Amm2$ ) is the intermediate phase between the rhombohedral ( $R3m$ ) and tetragonal ( $P4mm$ ) phases, thus the polarization rotation mechanism is applicable for the MPB composition of this BZT- $x$ BCT ferroelectric solid solution [103].

From the first principle DFT calculations, we have observed a strong phase competition around the MPB and the orthorhombic phase is stabilized as the ground state for a narrow composition range similar to previous path integral Monte Carlo quantum mechanical simulation result [53]. The local structure in the orthorhombic ( $Amm2$ ) phase is expected to be more disordered/fragmented than that of BT and allows easier fluctuations of the polarization BZT- $x$ BCT system around MPB [53]. The prominent CP can be evidence of the existence of local polar structure in BZT- $x$ BCT by Raman scattering. So, the presence of the orthorhombic ( $Amm2$ ) phase induces large fluctuations of the polarization, which gives rise to low energy barrier between the  $Amm2$  and  $P4mm$  ferroelectric phases (the energy difference between  $Amm2$  and  $P4mm$  phases is 7 meV per f.u. as observed from DFT calculations),

leading to easy polarization rotations. In short, the easy polarization rotation is responsible for high piezoelectric properties around the MPB region, which may be the necessary condition as proposed by Acosta et al. [52].

The extrinsic contribution of domain switching can also further flatten the polarization anisotropy energy [54]. It is well established that ferroelectric materials belonging to either tetragonal or rhombohedral crystal structure can have pinned domains, however for the coexistence phases the domain do switch [111]. The coexistence of  $Amm2 + P4mm$  phases show significant domain switching with limited intergranular constraints and manifest significant strain. The domain wall motions between different phases of different symmetry ( $Amm2 + P4mm$  phases in the present case), further reduces the free energy barrier to interface tension and strengthen the electro mechanical response [111]. *The question then arises, why are the functional properties a maximum for  $x=0.5$ ?*

From the XRD data, we have observed the discontinuity in the cell parameters and unit cell volume (around  $x=0.5$ ) representing a 1<sup>st</sup> order phase transitions, which indicate the critical point, where the piezoelectric coefficient is maximum [112]. Pramanic and co-workers based on *in situ* XRD experiment demonstrated that the decrease in tetragonality ( $c/a-1$ ) is well correlated with enhanced non-180° (ferroelectric/ferroelastic) domain wall motion, which significantly enhanced the piezoelectric properties [113]. The decrease of tetragonality is associated with enhanced domain wall motion, which influence the piezoelectric and dielectric properties [31,113]. From XRD data it has been observed that, the tetragonality decreases with increasing BZT concentrations with a minima around  $x=0.5$ . So, the domain wall contribution increases with the decreasing the BCT concentration, and the maximum contribution of the domain wall motion is observed around  $x=0.5$ , which is further responsible for the enhancement of the piezoelectric properties. The motion of domain walls in BZT- $x$ BCT is also in agreement with the CP behaviour observed in Raman scattering.

In the BZT- $x$ BCT system, the tetragonal (i.e., BCT;  $x=1.0$ ) ferroelectric domains have long-range order and the local structural heterogeneity tries to break the long range polar order with an increase in the BZT concentration (i.e., due to the increase in Zr concentration) [49]. However, the local structural heterogeneity does not impact the long range polarization of the ferroelectric (tetragonal) phase up to  $x=0.6$ . In the MPB compositions ( $0.45 \leq x \leq 0.55$ ), the local structural heterogeneity creates heterogeneous/nano-polar regions (PNRs) as observed by the relaxor ferroelectric nature from temperature dependent dielectric data. The local heterogeneous PNRs favours the orthorhombic phase due to large fluctuations of its polarization within the macroscopic  $Amm2$  phase. This supports a previous work, which shows the enhancement of piezoelectric properties by introducing a structural heterogeneity at the local scale [43]. Although the orthorhombic phase exist in the MPB region, at the critical composition ( $x=0.5$ ), the interfacial energy favours the transformation/alignment of the local polar nanoregions along the long-range polarization of the tetragonal state, which tends to minimize the polarization discontinuity. Thus, at the critical composition, the critical interfacial energy (the interface energy such as electrostatic, elastic and gradient energy) leads to the further flattening of the free energy profile so that the enhancement of the piezoelectric properties is observed for  $x=0.5$ .

Thus, the enhancement of the piezoelectric properties for 0.5BZT-0.5BCT is due to the combined and cooperative contributions such as (i) easy polarization rotation, (ii) maximum domain wall motion and critical interfacial energy due to the structural heterogeneity at the critical composition and (iii) the emergence of PNRs due to relaxor behaviour, which gives rise to very strong eletromechanical coupling. Thus, the induction of the structural

heterogeneity at the critical composition can be used as a guide to further improve the functional properties of the ferroelectric and multiferroic systems.

## V. CONCLUSIONS

The  $(1-x)\text{Ba}(\text{Zr}_{0.2}\text{Ti}_{0.8})\text{O}_3-x(\text{Ba}_{0.7}\text{Ca}_{0.3})\text{TiO}_3$  ( $0.3 \leq x \leq 1.0$ ) samples were thoroughly investigated near the MPB for their enhanced functional properties. The effect of compositions, especially near the MPB has been studied to correlate the structure, microstructure, dielectric, ferroelectric and piezoelectric properties. X-ray diffraction and Raman spectroscopy studies indicate a structural phase transition from a single rhombohedral ( $R3m$ ) phase with  $x \leq 0.4$  to tetragonal ( $P4mm$ ) phase for  $x \geq 0.6$  through a multiphase coexistence region of ( $Amm2+P4mm$ ) for  $0.45 \leq x \leq 0.55$ . First principle density functional theory calculations confirm the phase competition behaviour in the coexistence region. The multiphase coexistence region with composition  $x=0.5$  shows an enhanced dielectric, ferroelectric and piezoelectric properties around the MPB region. With the increase in BCT content,  $2P_r$  and  $d_{33}$  values increase and reach maximum values for  $x=0.5$ , then decreases with a further increase in the BCT concentration. The enhancement of the piezoelectric properties around the MPB can be attributed to the combined and cooperative contributions from easy polarization rotation and maximum domain wall motion due to the structural heterogeneity. The large dielectric permittivity, saturated hysteretic polarization and  $d_{33}$  values make them suitable for the replacement of Pb-based materials and have strong potential to be utilized in information and/or energy storage and electromechanical devices.

## ACKNOWLEDGEMENTS

SD and DKP acknowledge Prof. Mois I Aroyo and Prof. Gotzon Madariaga, Dpto. Física de la Materia Condensada, Universidad del País Vasco for fruitful discussion on the structural analysis. We acknowledge Prof. Rajeev Ranjan for his valuable suggestions on the Rietveld refinement analysis. DKP acknowledges support from the U. S. Department of Energy (DOE) under Grant No. DE-SC0002136. PDR acknowledges the Center for Nanophase Materials Sciences, which is a DOE Office of Science User Facility. C. C. acknowledges support from the Spanish Ministry of Science, Innovation, and Universities under the “Ramón y Cajal” fellowship RYC2018-024947-I. Computational resources and technical assistance were provided by the Australian Government and the Government of Western Australia through Magnus under the National Computational Merit Allocation Scheme and The Pawsey Supercomputing Centre.

## References

- [1] B. Jaffe, W. R. Cook, and H. Jaffe, *Piezoelectric Ceramics* (Academic press, London, 1971).
- [2] K. Uchino, *Advanced Piezoelectric Materials: Science and Technology* (Woodhead Publishing, USA, 2010).
- [3] A. K. Kalyani, H. Krishnan, A. Sen, A. Senyshyn, and R. Ranjan, *Phys. Rev. B* **91**, 024101 (2015).

- [4] J. Rödel, W. Jo, K. T. P. Seifert, E. M. Anton, T. Granzow, and D. Damjanovic, *J. Am. Ceram. Soc.* **92**, 1153 (2009).
- [5] Y. S. Sung, J. M. Kim, J. H. Cho, T. K. Song, M. H. Kim, H. H. Chong, T. G. Park, D. Do, and S. S. Kim, *Appl. Phys. Lett.* **96**, 022901 (2010).
- [6] Y. Saito, H. Takao, T. Tani, T. Nonoyama, K. Takatori, T. Homma, T. Nagaya, and M. Nakamura, *Nature* **432**, 84 (2004).
- [7] W. Liu and X. Ren, *Phys. Rev. Lett.* **103**, 257602 (2009).
- [8] A. A. Heitmann and G. A. Rossetti, *J. Am. Ceram. Soc.* **97**, 1661 (2014).
- [9] A. K. Kalyani, K. Brajesh, A. Senyshyn, and R. Ranjan, *Appl. Phys. Lett.* **104**, 252906 (2014).
- [10] Y. Ishibashi and M. Iwata, *Jpn. J. Appl. Phys.* **37**, L985 (1998).
- [11] M. Iwata, H. Orihara, and Y. Ishibashi, *Jpn. J. Appl. Phys.* **40**, 703 (2001).
- [12] M. Iwata and Y. Ishibashi, *Jpn. J. Appl. Phys.* **38**, 5670 (1999).
- [13] See Supplemental Material at [URL] for additional details information on X Ray Diffraction, Raman Spectroscopy, Surface Morphology and EDX Spectra, Dielectric Properties, Polarization Rotation Model, and a brief Review on the Crystal Structure and Symmetry of BZT-*x*BCT system.
- [14] W. Li, Z. Xu, R. Chu, P. Fu, and G. Zang, *Phys. B: Condens. Matter* **405**, 4513 (2010).
- [15] V. S. Puli, A. Kumar, D. B. Chrisey, M. Tomozawa, J. F. Scott, and R. S. Katiyar, *J. Phys. D: Appl. Phys.* **44**, 395403 (2011).
- [16] B. Li, J. E. Blendell, and K. J. Bowman, *J. Am. Ceram. Soc.* **94**, 3192 (2011).
- [17] M. C. Ehmke, S. N. Ehrlich, J. E. Blendell, and K. J. Bowman, *J. Appl. Phys.* **111**, 124110 (2012).
- [18] I. K. Jeong and J. S. Ahn, *Appl. Phys. Lett.* **101**, 99 (2012).
- [19] W. Li, Z. Xu, R. Chu, P. Fu, and G. Zang, *Curr. Appl. Phys.* **12**, 748 (2012).
- [20] D. S. Keeble, F. Benabdallah, P. A. Thomas, M. Maglione, and J. Kreisel, *Appl. Phys. Lett.* **102**, 092903 (2013).
- [21] B. Li, M. C. Ehmke, J. E. Blendell, and K. J. Bowman, *J. Eur. Ceram. Soc.* **33**, 3037 (2013).
- [22] V. S. Puli, D. K. Pradhan, W. Pérez, and R. S. Katiyar, *J. Phys. Chem. Solids* **74**, 466 (2013).
- [23] M. Sindhu, N. Ahlawat, S. Sanghi, R. Kumari, and A. Agarwal, *J. Appl. Phys.* **114**, 164106 (2013).

- [24] D. Fu, Y. Kamai, N. Sakamoto, N. Wakiya, H. Suzuki, and M. Itoh, *J. Phys. Condens. Matter* **25**, 425901 (2013).
- [25] I. Coondoo, N. Panwar, H. Amorín, M. Alguero, and A. L. Kholkin, *J. Appl. Phys.* **113**, 214107 (2013).
- [26] A. B. Haugen, J. S. Forrester, D. Damjanovic, B. Li, K. J. Bowman, and J. L. Jones, *J. Appl. Phys.* **113**, 0141103 (2013).
- [27] Y. Tian, L. Wei, X. Chao, Z. Liu, and Z. Yang, *J. Am. Ceram. Soc.* **96**, 496 (2013).
- [28] E. V. Ramana, A. Mahajan, M. P. F. Graça, S. K. Mendiratta, J. M. Monteiro, and M. A. Valente, *Mater. Res. Bull.* **48**, 4395 (2013).
- [29] J. Gao, L. Zhang, D. Xue, T. Kimoto, M. Song, L. Zhong, and X. Ren, *J. Appl. Phys.* **115**, 054108 (2014).
- [30] P. Mishra, Sonia, and P. Kumar, *Ceram. Int.* **40**, 14149 (2014).
- [31] G. Tutuncu, B. Li, K. Bowman, and J. L. Jones, *J. Appl. Phys.* **115**, 144104 (2014).
- [32] Z. Sun, Y. Pu, Z. Dong, Y. Hu, P. Wang, X. Liu, and Z. Wang, *Mater. Sci. Eng. B* **185**, 114 (2014).
- [33] H. Guo, B. K. Voas, S. Zhang, C. Zhou, X. Ren, S. P. Beckman, and X. Tan, *Phys. Rev. B* **90**, 014103 (2014).
- [34] K. Brajesh, K. Tanwar, M. Abebe, and R. Ranjan, *Phys. Rev. B* **92**, 224112 (2015).
- [35] J. P. Praveen, T. Karthik, A. R. James, E. Chandrakala, S. Asthana, and D. Das, *J. Eur. Ceram. Soc.* **35**, 1785 (2015).
- [36] K. Brajesh, M. Abebe, and R. Ranjan, *Phys. Rev. B* **94**, 104108 (2016).
- [37] P. Adhikari, R. Mazumder, and S. Abhinay, *J. Electroceram.* **37**, 127 (2016).
- [38] P. Adhikari, R. Mazumder, and G. K. Sahoo, *Ferroelectrics* **490**, 60 (2016).
- [39] L. Zhang, X. Ren, and M. A. Carpenter, *Phys. Rev. B* **95**, 054116 (2017).
- [40] H. Kaddoussi, A. Lahmar, Y. Gagou, B. Manoun, J. N. Chotard, J. L. Dellis, Z. Kutnjak, H. Khemakhem, B. Elouadi, and M. E. Marssi, *J. Alloys Compd.* **713**, 164 (2017).
- [41] A. R. Montero, F. R. Marcos, L. Pardo, A. D. Campo, R. L. -Juárez, and M. E. V. -Castrejón, *J. Mater. Chem. A* **6**, 5419 (2018).
- [42] B. C. Keswani, S. I. Patil, A. R. James, Y. D. Kolekar, and C. V. Ramana, *Ceram. Int.* **44**, 20921 (2018).
- [43] A. Akbarzadeh, K. Brajesh, Y. Nahas, N. Kumar, S. Prokhorenko, D. Swain, S. Prosandeev, R. Walter, I. Kornev, J. Íñiguez, B. Dkhil, R. Ranjan, and L. Bellaiche, *Phys. Rev. B* **98**, 104101 (2018).

- [44] A. R. Jayakrishnan, K. V. Alex, A. Thomas, J. P. B. Silva, K. Kamakshi, N. Dabra, K. C. Sekhar, J. A. Moreira, and M. J. M. Gomes, *Ceram. Int.* **45**, 5808 (2019).
- [45] D. A. Ochoa, A. R. Montero, F. Suñol, M. E. V. Castrejón, L. Pardo, and J. E. García, *J. Alloys Compd.* **774**, 410 (2019).
- [46] A. B. Swain, D. Murali, B. R. K. Nanda, and P. Murugavel, *Phys. Rev. Appl.* **11**, 044007 (2019).
- [47] A. Mondal, P. Saha, B. Ghosh, M. Sahu, G. D. Mukherjee, R. Ranjan, and K. Brajesh, *J. Am. Ceram. Soc.* **103**, 5259 (2020).
- [48] Y. Yang, W. Wang, X. Chen, Y. Wang, D. Gao, and D. Xue, *J. Mater. Sci.* **55**, 16890 (2020).
- [49] K. Dey, A. Ahad, K. Gautam, A. Tripathy, S. S. Majid, S. Francoual, C. Richter, M. N. Singh, A. Sagdeo, E. Welter, and others, *Phys. Rev. B* **103**, L100205 (2021).
- [50] M. Acosta, N. Novak, G. A. Rossetti, and J. Rödel, *Appl. Phys. Lett.* **107**, 142906 (2015).
- [51] J. Gao, X. Hu, L. Zhang, F. Li, L. Zhang, Y. Wang, Y. Hao, L. Zhong, and X. Ren, *Appl. Phys. Lett.* **104**, 252909 (2014).
- [52] M. Acosta, N. Khakpash, T. Someya, N. Novak, W. Jo, H. Nagata, G. A. Rossetti, and J. Rödel, *Phys. Rev. B* **91**, 104108 (2015).
- [53] Y. Nahas, A. Akbarzadeh, S. Prokhorenko, S. Prosandeev, R. Walter, I. Kornev, J. Íñiguez, and L. Bellaiche, *Nat. Commun.* **8**, 15944 (2017).
- [54] K. Datta, K. Brajesh, R. Ranjan, and B. Mihailova, *Phys. Rev. B* **102**, 060102(R) (2020).
- [55] S. Dash, H. S. Mohanty, K. Bhoi, R. Kant, A. Kumar, R. Thomas, and D. K. Pradhan, *J. Mater. Sci. Mater. Electron.* **29**, 20820 (2018).
- [56] J. P. Perdew, K. Burke, and M. Ernzerhof, *Phys. Rev. Lett.* **77**, 3865 (1996).
- [57] G. Kresse and J. Furthmüller, *Phys. Rev. B* **54**, 11169 (1996).
- [58] G. Kresse and D. Joubert, *Phys. Rev. B* **59**, 1758 (1999).
- [59] P. E. Blöchl, *Phys. Rev. B* **50**, 17953 (1994).
- [60] C. Cazorla and M. Stengel, *Phys. Rev. B* **90**, 020101(R) (2014).
- [61] C. Cazorla and M. Stengel, *Phys. Rev. B* **92**, 214108 (2015).
- [62] C. Cazorla and J. Íñiguez, *Phys. Rev. B* **88**, 214430 (2013).
- [63] C. Cazorla, O. Diéguez, and J. Íñiguez, *Sci. Adv.* **3**, e1700288 (2017).
- [64] M. Abebe, K. Brajesh, A. Mishra, A. Senyshyn, and R. Ranjan, *Phys. Rev. B* **96**,

- 014113 (2017).
- [65] S. P. Singh, R. Ranjan, A. Senyshyn, D. Trots, and H. Boysen, *J. Phys. Condens. Matter* **21**, 375902 (2009).
  - [66] M. M. Rahaman, T. Imai, T. Sakamoto, S. Tsukada, and S. Kojima, *Sci. Rep.* **6**, 23898 (2016).
  - [67] M. M. Rahaman, T. Imai, T. Sakamoto, M. A. Helal, S. Tsukada, and S. Kojima, *J. Alloys Compd.* **735**, 1063 (2018).
  - [68] N. K. Karan, R. S. Katiyar, T. Maiti, R. Guo, and A. S. Bhalla, *J. Raman Spectrosc.* **40**, 370 (2009).
  - [69] M. DiDomenico Jr, S. H. Wemple, S. P. S. Porto, and R. P. Bauman, *Phys. Rev.* **174**, 522 (1968).
  - [70] G. Burns and B. A. Scott, *Solid State Commun.* **9**, 813 (1971).
  - [71] P. Hermet, M. Veithen, and P. Ghosez, *J. Phys. Condens. Matter* **21**, 215901 (2009).
  - [72] K. Laabidi, M. D. Fontana, and B. Jannot, *Solid State Commun.* **76**, 765 (1990).
  - [73] N. V. Dang, T. D. Thanh, L. V. Hong, V. D. Lam, and T. -L. Phan, *J. Appl. Phys.* **110**, 043914 (2011).
  - [74] C. J. Xiao, C. Q. Jin, and X. H. Wang, *Mater. Chem. Phys.* **111**, 209 (2008).
  - [75] E. Buixaderas, M. Berta, L. Kozielski, and I. Gregora, *Phase Transitions* **84**, 528 (2011).
  - [76] G. Singh, V. Sathe, and V. S. Tiwari, *J. Electron. Mater.* **46**, 4976 (2017).
  - [77] I. G. Siny, R. Tao, R. S. Katiyar, R. Guo, and A. S. Bhalla, *J. Phys. Chem. Solids* **59**, 181 (1998).
  - [78] U. Fano, *Phys. Rev.* **124**, 1866 (1961).
  - [79] D. L. Rousseau and S. P. S. Porto, *Phys. Rev. Lett.* **20**, 1354 (1968).
  - [80] A. Pinczuk, E. Burstein, and S. Ushioda, *Solid State Commun.* **7**, 139 (1969).
  - [81] J. -H. Ko, T. H. Kim, K. Roleder, D. Rytz, and S. Kojima, *Phys. Rev. B* **84**, 094123 (2011).
  - [82] M. D. Fontana, N. Kokanyan, and T. H. Kauffmann, *J. Phys. Condens. Matter* **32**, 285403 (2020).
  - [83] S. Banerjee, D. -I. Kim, R. D. Robinson, I. P. Herman, Y. Mao, and S. S. Wong, *Appl. Phys. Lett.* **89**, 223130 (2006).
  - [84] D. K. Pradhan, H. S. Mohanty, S. Kumari, K. Bhoi, N. Tang, Ravikant, M. M. Rahaman, D. K. Pradhan, A. Kumar, D. A. Gilbert, and P. D. Rack, *J. Mater. Chem. C*

- 9, 12694 (2021).
- [85] G. Burns and B. A. Scott, Phys. Rev. B **7**, 3088 (1973).
- [86] M. M. Rahaman, T. Imai, T. Sakamoto, and S. Kojima, Integr. Ferroelectr. **185**, 22 (2017).
- [87] F. R. -Marcos, A. D. Campo, P. Marchet, and J. F. Fernández, Nat. Commun. **6**, 6594 (2015).
- [88] D. H. Suh, D. H. Lee, and N. K. Kim, J. Eur. Ceram. Soc. **22**, 219 (2002).
- [89] X. G. Tang, K. H. Chew, and H. L. W. Chan, Acta Mater. **52**, 5177 (2004).
- [90] K. Uchino and S. Nomura, Ferroelectrics **44**, 55 (1982).
- [91] G. D. Adhikary, D. K. Khatua, A. Mishra, A. De, N. Kumar, S. Saha, U. Shankar, A. Senyshyn, B. N. Rao, and R. Ranjan, Phys. Rev. B **100**, 134111 (2019).
- [92] R. E. Eitel, C. A. Randall, T. R. Shrout, P. W. Rehrig, W. Hackenberger, and S. -E. Park, Jpn. J. Appl. Phys. **40**, 5999 (2001).
- [93] A. A. Bokov and Z. G. Ye, Phys. Rev. B **65**, 144112 (2002).
- [94] R. Pandey, B. Narayan, D. K. Khatua, S. Tyagi, A. Mostaed, M. Abebe, V. Sathe, I. M. Reaney, and R. Ranjan, Phys. Rev. B **97**, 224109 (2018).
- [95] A. B. -Holder, H. Beige, and G. Völkel, Phys. Rev. B **79**, 184111 (2009).
- [96] V. V. Shvartsman and D. C. Lupascu, J. Am. Ceram. Soc. **95**, 1 (2012).
- [97] B. C. Keswani, D. Saraf, S. I. Patil, A. Kshirsagar, A. R. James, Y. D. Kolekar, and C. V. Ramana, J. Appl. Phys. **123**, 204104 (2018).
- [98] C. Zhao, W. Wu, H. Wang, and J. Wu, J. Appl. Phys. **119**, 024108 (2016).
- [99] Y. Tian, X. Chao, L. Wei, P. Liang, and Z. Yang, J. Appl. Phys. **113**, 184107 (2013).
- [100] M. Zakhosheva, L. A. Schmitt, M. Acosta, H. Guo, W. Jo, R. Schierholz, H. J. Kleebe, and X. Tan, Phys. Rev. Appl. **3**, 064018 (2015).
- [101] D. Damjanovic, Appl. Phys. Lett. **97**, 062906 (2010).
- [102] M. E. Lines and A. M. Glass, *Principles and Applications of Ferroelectrics and Related Materials* (Oxford university press, New York, 2001).
- [103] H. Fu and R. E. Cohen, Nature **403**, 281 (2000).
- [104] F. Li, D. Lin, Z. Chen, Z. Cheng, J. Wang, C. Li, Z. Xu, Q. Huang, X. Liao, L. -Q. Chen, T. R. Shrout, and S. Zhang, Nat. Mater. **17**, 349 (2018).
- [105] F. Cordero, F. Craciun, M. Dinescu, N. Scarisoreanu, C. Galassi, W. Schranz, and V. Soprunyuk, Appl. Phys. Lett. **105**, 232904 (2014).

- [106] M. Ahart, M. Somayazulu, R. E. Cohen, P. Ganesh, P. Dera, H. Mao, R. J. Hemley, Y. Ren, P. Liermann, and Z. Wu, *Nature* **451**, 545 (2008).
- [107] B. Noheda, *Curr. Opin. Solid State Mater. Sci.* **6**, 27 (2002).
- [108] N. Zhang, H. Yokota, A. M. Glazer, Z. Ren, D. A. Keen, D. S. Keeble, P. A. Thomas, and Z. G. Ye, *Nat. Commun.* **5**, 5231 (2014).
- [109] A. K. Singh and D. Pandey, *Phys. Rev. B* **67**, 064102 (2003).
- [110] D. L. Orantapong, B. Noheda, Z. G. Ye, P. M. Gehring, J. Toulouse, D. E. Cox, and G. Shirane, *Phys. Rev. B* **65**, 144101 (2002).
- [111] J. Y. Li, R. C. Rogan, E. Üstündag, and K. Bhattacharya, *Nat. Mater.* **4**, 776 (2005).
- [112] Z. Kutnjak, J. Petzelt, and R. Blinc, *Nature* **441**, 956 (2006).
- [113] A. Pramanick, D. Damjanovic, J. E. Daniels, J. C. Nino, and J. L. Jones, *J. Am. Ceram. Soc.* **94**, 293 (2011).